THRESHOLD STRENGTH CERAMIC DENTAL CROWNS BY DIRECT INK WRITING

By

MORGAN CORNISH

Bachelor of Science in Ceramic Engineering

Missouri University of Science and Technology

Rolla, MO

2018

Submitted to the Faculty of the

Graduate College of the
Oklahoma State University
in partial fulfillment of
the requirements for
the Degree of
MASTER OF SCIENCE
May, 2020

THRESHOLD STRENGTH CERAMIC DENTAL CROWNS BY DIRECT INK WRITING

Thesis Approved:

Dr. Jim Smay

Thesis Adviser
Dr. Jim Smay

Dr. Pankaj Sarin

Dr. Pankaj Sarin

Dr. Do Young Kim

Dr. Do Young Kim

ACKNOWLEDGEMENTS

Dr. James Smay
Dr. Pankaj Sarin
Dr. Do Young Kim
Dr. Daniel Lowry, Yang Shi, Dr. Lukasz Witek
The entire MSE department
Jennifer Holloway
Ricky and Kelly Cornish

Name: MORGAN CORNISH

Date of Degree: MAY 2020

Title of Study: THRESHOLD STRENGTH CERAMIC DENTAL CROWNS BY DIRECT INK WRITING

Major Field: MATERIALS SCIENCE AND ENGINEERING

ABSTRACT

A functionally graded threshold strength dental ceramic consisting of a ZrO_2 core coated with Al_2O_3 strengthened ZrO_2 (ASZ) is produced by direct ink writing (DIW). The two materials are printed as a core-shell disk and co-sintered to induce a threshold stress caused by a mismatch in coefficient of thermal expansion (CTE). Biaxial flexure testing with a piston-on-3-ball procedure outlined in ISO 6872/2008 is used to assess the flexural strength of the composite disks alongside monolithic samples of the three constituent materials (ZrO_2, Al_2O_3, and ASZ). The threshold strength ceramic possesses the greatest average flexural strength (670.22 ± 69.74 MPa) of the four materials tested, and possesses significantly greater flexural strength than several ceramics commonly used as crown materials. Additionally, Weibull analysis is used to provide a quantifiable metric for failure reliability, where the composite samples outperform the other tested materials in both Weibull modulus ($m = 8.60$) and characteristic strength ($\sigma_0 = 737.15$ MPa). In light of these results, functionally graded threshold strength ceramics produced via robocasting show great promise as potential dental ceramics.

TABLE OF CONTENTS

Chapter Page

LIST OF TABLES

Table Page

LIST OF FIGURES

Figure Page

1. INTRODUCTION

1.1 Motivation

The computer aided design and manufacture (CAD/CAM) of ceramic and glass-ceramic dental prosthetics, both anterior and posterior, has become commonplace in modern dentistry. Zirconia (ZrO_2) is translucent with good mechanical properties, making it the ceramic of choice for anterior restorations where esthetics are a critical factor, whereas Al_2O_3 is more suitable for posterior bridges and crowns. The manufacturing technique in either case (or for glass ceramics) is to mill the prosthetic from a billet of bisque fired material followed by a final sintering to full density. While sophisticated 5-axis computer numerical control (CNC) milling machines produce impressive geometries, they also introduce a significant amount of microstructural damage to the ceramic than can persist in the sintered product. Despite widespread acceptance and success of CNC milled ceramic restorations, ceramics occasionally fail prematurely based on the presence of surface flaws and the CNC crowns have always been plagued by unexpected catastrophic failure. As a mitigation strategy, toughening ZrO_2 with up to 20% Al_2O_3 is common, but even this mixture is susceptible to damage that might be incurred during installation when dentists "roughen" the surface with a diamond bur prior to final placement. Here, we explore use of an additive manufacturing process to create dental crowns with a heterogeneous composition consisting of a low thermal expansion (thin) shell atop a high thermal expansion (thick) core to induce a residual compressive stress at the surface of the dental prosthetic and ensure a minimum threshold strength for the ceramic.(1-12)

Since the invention of stereolithography in 1983, additive manufacturing has been the subject of cutting edge research, with ceramics being introduced to the materials pallet in the late 1990's. Direct ink writing, an additive manufacturing process often referred to as robocasting(13) when printing ceramics, is being investigated as a means of manufacturing these threshold strength ceramic dental prosthetics. Robocasting consists of extruding a colloidal gel "ink" to "write/draw" lines of ink to produce a layer of "green" ceramic. Sequential printing of layers yields the 3-D shape. Robocasting allows for precise control of composition with respect to printing space, allowing for the production of 3D functionally graded materials. Without this technology, it would be impossible, or at least extremely difficult, to produce a conformally graded ceramic structure that could possibly induce a threshold strength below which failure probability is zero.

In this study, alumina stabilized zirconia (ASZ) was used as the coating material for yittria stabilized zirconia (YSZ) samples to take advantage of the CTE mismatch and create threshold strength ceramic samples. These samples were printed using both alumina and zirconia inks in a 2-tip configuration. Additionally, baseline samples of alumina, YSZ, and alumina stabilized zirconia (ASZ) were printed. These samples were mechanically characterized with biaxial flexure and evaluated using Weibull statistics and Vickers indentation.

1.2 Application

Al_2O_3 and ZrO_2 are widely used as dental ceramics for prosthetics like crowns and bridges. They possess much higher flexural strength values than other dental materials such as glass ceramics or porcelain, and with the aid of doping these materials have the ability to alter their shading to better match the patient's existing teeth.(14-24) An example of this dopant shading is shown in Figure 1 below, where a stabilized zirconia dental ceramic was doped using iron oxide.(24)

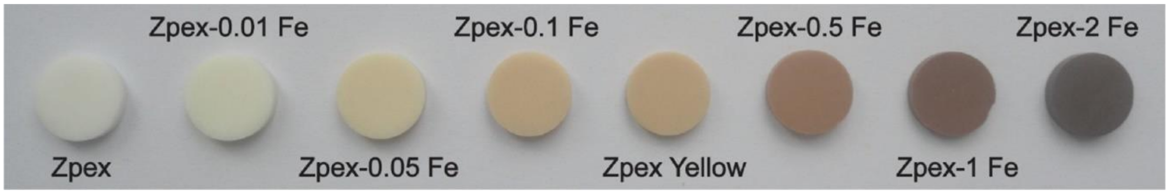

Figure 1: Shading of stabilized zirconia using iron oxide dopant.(24)

Despite these materials showing large strength values, their downfall is their low fracture toughness. Ceramics are, by nature, brittle. Additionally, the state of the surface of monolithic ceramics is often unknowable due to process inherent microcracking. This requires their strengths to be stated as a statistical value with a fairly wide distribution. Nevertheless, fracture toughness has been improved by strategies such as phase-transformation toughening and blending of ceramics to cause a tortuous crack path during fracture. More recently, threshold strength materials have shown promise in producing ceramic structures with predictable failure.(1, 2, 9-12) Threshold strength materials use an intentionally engineered internal stress that places the surface into compression, thereby closing or reducing the size of surface flaws. This compressive stress must be overcome by a tensile stress of equal magnitude in order to begin growing the surface flaws. Since failure can only occur in brittle materials when a flaw grows to a critical size, these materials ensure a zero percent failure probability below the threshold stress requirement. If a dental crown can be produced that has a threshold strength in excess of the stress profiles exhibited by everyday human mastication, it would significantly increase the period of time before these restorations fail due to cyclic fatigue.

Therefore, producing a threshold strength dental crown could eliminate the growth of subcritical surface flaws due to mastication fatigue. This will vastly increase the lifespan and degree of reliability of these dental ceramic restorations and narrow the causes of failure to gradual wear and high-stress impact events. Due to the promise seen in this practical application, a conformal alumina-zirconia system is investigated to evaluate the potential of the threshold strength effect on the fracture reliability of ceramic dental restorations.

1.3 Background

1.3.1 Direct Ink Writing

3D printing refers to any process in which a three-dimensional object is manufactured by means of slicing a digital model into thin, two-dimensional layers followed by the deposition of a material in a layer-by-layer fashion. Many 3D printing techniques (e.g., fused deposition modeling (FDM), direct ink writing (DIW), selective laser sintering (SLS), laminated object manufacturing (LOM), etc.) have been invented, but the earliest technique can be traced to the 1983 invention of stereolithography where selective photopolymerization using a scanning laser in a resin bath builds objects layer-by-layer. The freedom to print any arbitrary shape without the need for specialized molds or tooling has changed manufacturing over the past three decades as the cost and time to manufacture a part has consistently declined while the materials pallet available has expanded to include many metals and ceramics in addition to thermoplastics and thermosets.

Direct ink writing, referred to as robocasting for ceramic materials, is a type of 3D printing that extrudes a filament of colloidal-gel ink from a deposition nozzle. This nozzle traces a tool path within each layer while assembling the 3D object in a layer-by-layer fashion. Direct ink writing can be used to print a wide variety of material systems like metals, ceramics, and thermoset polymers, to name a few. Manufacturing ceramic components using reductive manufacturing techniques is often time consuming and extremely expensive due to tooling costs. Additionally, final geometry is extremely limited by traditional forming processes for these technical ceramics. Fortunately, robocasting can produce ceramic components with highly complex geometry with little to no need for post-firing machining, saving time and cost.

The direct ink writing production of a ceramic part consists of the following work flow: *i*) computer aided design (CAD) model of the object to be printed and production of instructions for the printer (g-code), *ii*) printing the model layer-by-layer from a suitably prepared ink(s), *iii*) drying the model to yield a green ceramic, and *iv*) sintering to produce a dense part. In *i*) the model is typically an .stl file format which estimates the surface of the object with triangular facets oriented normal to the model surface. The .stl model resolution can be modified by changing the maximum size of these triangles allowed to describe the surface, which increases the number of facets used to define object geometry. A visual representation of a high resolution model vs a low resolution model can be seen in Figure 2 below.(25)

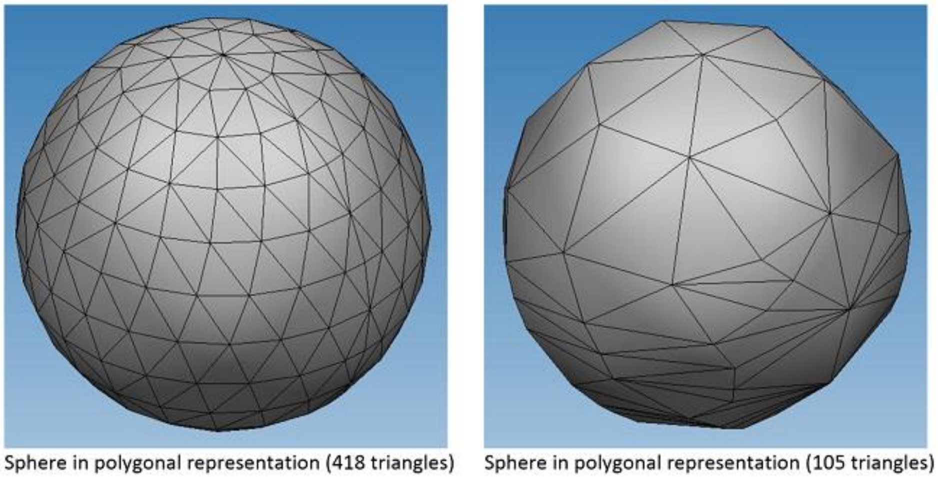

Figure 2: High vs low resolution .stl model.(25)

The .stl file is then oriented in XYZ space and sliced along the Z-axis into layers whose thickness correspond to the height of the filament deposition. A toolpath is generated for each of the slices in the form of computer numerical control (CNC) instructions or g-code. Finally, these instructions are sent to the 3D printer and the object is printed. The Smay lab group has developed a direct ink writing system that is capable of printing multiple inks through discrete nozzles.(26-33) This capability allows for the printing of ceramic components with spatially controlled composition.

More recently, the Smay group has developed the software required to create ceramic parts with a coating, or candy shell (CS), layer conformal to the object surface. Figure 3 provides a visual representation of a core-shell calculation for a ceramic dental bridge. Here, the occlusal surface of the bridge is pointed toward the build platform and a slice has been calculated to reveal the interior (core) of the composite structure (the translucent yellow part) and the shell (opaque white part). Paying careful attention to the highlighted (blue) layer, one can see that though the shell is of uniform thickness in 3D, slicing reveals that the toolpath will be of non-uniform width in 2D for any given layer. Less obvious is that composition in the layer is influenced by the 3D distance from and exterior surface that may be above or below the layer.

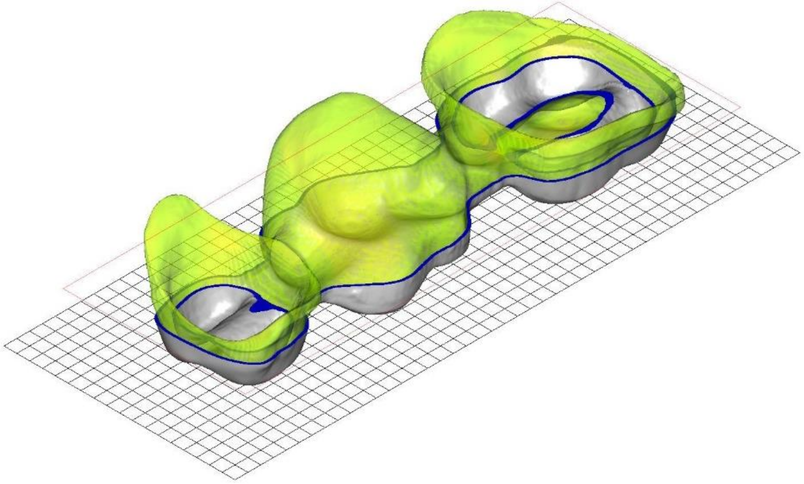

Figure 3: Rendering of a conformal core-shell three-tooth bridge.

Once this model has been produced, it will undergo slice and fill operations and will produce the G-code necessary for a multi-material print using two or more discreet tips. The G-code is then sent to the printer, and the ceramic bridge is printed. Upon completion, the crown is removed and dried slowly to prevent drying stresses and warpage. At this stage the bridge is referred to as a green body, or a formed object comprised of weakly bound ceramic powder. After firing the green body at the materials designated sintering temperature, the resulting product is a strong, densified ceramic bridge.

The direct ink writing process provides some considerable advantages over traditional ceramic manufacturing techniques. For technical ceramics like alumina and zirconia, most forming techniques are severely geometrically limited. Typically, additives such as binders and sintering aids are added to ceramic powders and are consolidated into a geometrically simple shape like a rod or tile via forming methods like extrusion or uniaxial pressing. They are then dried and sintered to their desired density. Finally, in order to produce a geometrically complex part, the sintered billet is then machined to its final shape. This comes at great cost to the manufacturer due to the high tooling costs and times associated with machining high hardness ceramic materials. Due to the brittle nature of ceramics, the material is extremely hard to machine without fatally damaging the part. Additionally, this process often reduces the strength and fracture toughness of the ceramic by exacerbating surface flaws. Alternatively, robocasting can be used to form the ceramic body to its final geometry before the sintering process, eliminating the need for machining and thus maintaining the materials strength and fracture toughness.

1.3.2 Colloidal Processing

Ink formulation for printing the threshold strength component is, perhaps, the most critical step of the process. The inks used in this study are concentrated colloidal gels consisting of aqueous mixtures of submicron ceramic powders and minimal polymeric processing chemicals. For successful printing, a pseudoplastic with yield stress rheology is necessary to facilitate flow through the deposition nozzle at moderate pressures and rapid setting after deposition to enable shape retention of the extrudate. Rheology, drying, binder burnout, and final sintering are highly sensitive to solids volume fraction (ϕ_{solids}) in the colloidal ink with maximizing ϕ_{solids} being the goal. Initial dispersion argues for low viscosity, stable colloidal suspensions, whereas extrusion and shape retention argue for high viscosity flocculated colloidal gels. Hence, an understanding of the underlying interparticle interaction forces and strategies for controlling them is important.

Both initial dispersion of the ceramic powders (first step) and subsequent controlled aggregation (final step) of ink preparation mediate the inter-particle forces described by the Deryagin, Landau, Verwey, Overbeek (DLVO) theory. Colloidal particles are attracted to one another by long range Van der Waals and Coulombic forces.(34, 35) Bare ceramic surfaces in water will hydrate, more or less, as a function of suspension pH creating a layer of immobile counter ions close to the surface (the Stern layer) and a diffuse cloud of ions (the double layer) than can induce an osmotic pressure to drive like-charged particles apart upon close approach. The thickness of the double layer and hence the range of the repulsive force is highly sensitive to ionic strength and the colloidal suspension is deemed "stable" if the magnitude and range of the repulsive force is sufficient to prevent aggregation (flocculation). Figure 4 below provides a visual representation of the total interaction energy between two particles as a function of interparticle distance.(36)

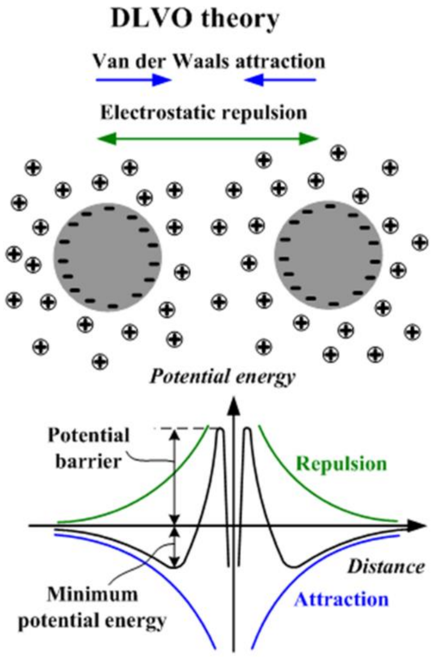

Figure 4: Diagram of DLVO Theory as function of interparticle distance.(36)

Additives to the aqueous phase can be adsorbed to the surface of the colloidal particles to introduce two methods for controlling interparticle interactions: steric and electrosteric. Steric interactions occur when adsorbed (typically hydrophilic) polymer brushes overlap and repel one another due to the decreased entropy. The extent and magnitude of the adsorbed polymer brush is an effective physical barrier to flocculation and is usually insensitive to ionic strength and pH. Electrosteric interactions combine the electrostatic and steric approaches by taking advantage of polyelectrolytes that dissociate in an aqueous solution to produce charged polymers. Because these polymers are charged, they can adhere to the Stern layer of particles and attract a double layer beyond the polymer chains, essentially combining both steric and electrostatic repulsion mechanisms. The thickness of the polymer chain layer can be controlled by manipulating the pH of the solution as well as the ionic strength. By controlling pH, one controls the extent to which the polyelectrolyte is allowed to dissociate. For example, if pH is high there are more free hydroxide groups to dissociate a hypothetical anionic polyelectrolyte, allowing it to adsorb. With more adsorbed polyelectrolytes there is a higher concentration of negative charges which creates a repulsive force between the adsorbed fibers themselves, thereby expanding the polymer coils and thickening the polymer layer. The reverse of this would occur when pH is low with very few hydroxide groups present, leading to a lower fraction of dissociated polyelectrolytes. With a lower concentration of negative charges there is less polymer-polymer repulsion and the chains tend toward a tighter coiled conformation, thereby decreasing the thickness of the polymer layer. A visual summary of the stabilization techniques discussed above can be viewed in Figure 5.(37)

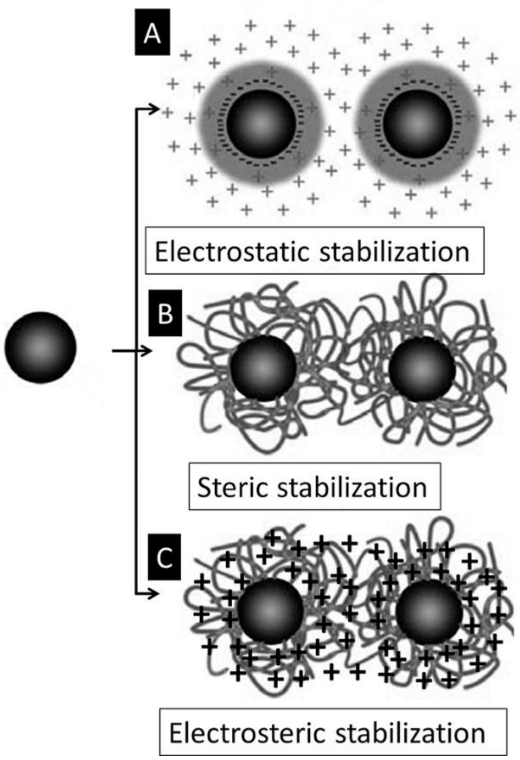

Figure 5: Summary of colloidal stabilization techniques.(37)

The ink production process involves making a well dispersed mixture using one of the stabilization methods above followed by gelling that mixture via flocculation to a degree where the desired rheology is achieved.(35, 38) In this study, ceramic powders are electosterically dispersed in an aqueous solution using an anionic polyelectrolyte and gelled by adding a flocculating agent comprised of cationic polyelectrolyte. Upon addition of the flocculant, the cationic polyelectrolyte becomes attracted to the anionic dispersant polymers. These positively charged polymers can bridge between the negatively charged polymer layers of the coated particles, causing them to stick together. As more and more particles stick together, a gel network begins to form and a viscous ink is created. The strength of this physical gel can be easily controlled by concentration and produces a shear-reversible gel that is very suitable for robocasting.

The rheology of concentrated colloidal suspensions and (especially) colloidal gels is highly non-Newtonian and of paramount importance in the development of new ink compositions. The rheological properties of each new ink needs to be thoroughly investigated in order to characterize their flow characteristics. A collection of rheological behaviors in terms of shear rate ($\dot{\gamma}$) vs shear stress (τ) is illustrated in Figure 6.(25) Pseudopastic with yield stress behavior indicates viscoelastic behavior with elastic modulus (G') > viscous modulus (G'') below a shear yield stress (τ_y). In this range the floc structure is stretched, but floc and interparticle bonds remain intact. Beyond the yield stress, the particle gel ruptures allowing shear flow where floc size decreases along with decreasing viscosity (η_{app}) and increasing $\dot{\gamma}$.(34) Ideally, τ_y is sufficient to prevent flow after deposition even when subjected to the forces from subsequent layers printed atop a resting layer. The connection between colloidal interaction forces, ink rheology, and printing is complex and highly dependent upon shear history. Nevertheless, the process can be estimated to proceed from i) a quiescent reservoir of colloidal ink to a ii) short duration exposure to a high shear field during extrusion to a iii) resting period as the colloidal gel network recovers and the extrudate becomes a portion of the printed part. These processes have been studied and described in detail elsewhere.(26-33, 35, 38-47)

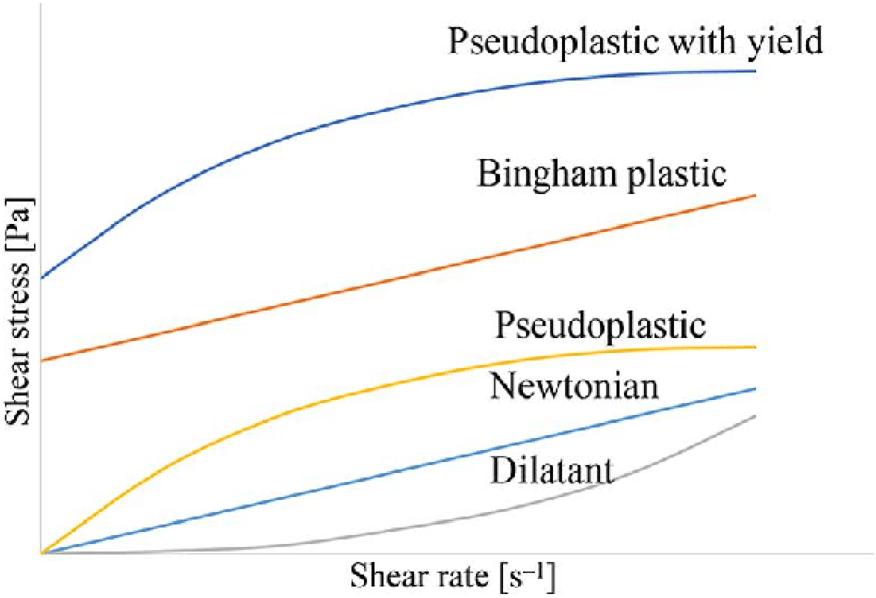

Figure 6: Collection of various rheological behaviors.(48)

1.3.3 Threshold Strength Ceramics

Threshold strength ceramics where developed by Fred Lange and colleagues in the late 1990's and early 2000's. They produced ceramic laminates and 3D architectures with a thin compressive outer layer that exhibited a threshold stress requirement below which the probability of failure is zero percent.(1, 2, 9, 10, 12, 49) The threshold stress is manufactured by intentionally producing a ceramic part with a residual compressive surface stress caused by a mismatch in shrinkage during the cooling after sintering. It was found that this shrinkage could be due to a difference in CTE between two different materials or a localized change in phase from a single material. In order to reach critical failure, enough tensile stress must be imparted onto the object that the threshold stress is overcome and then any additional tensile stress can then cause flaw growth to a critical size.

Lange et al. has shown that the residual differential thermal strain, ε_r, found between laminates of two materials with differing thermal expansion coefficients is expressed as

$$\varepsilon_r = \int_{T_i}^{T_f} (\alpha_c - \alpha_t) dT \tag{1}$$

where T_i and T_f are the initial and final temperatures upon cooling, α_c and α_t are the thermal expansion coefficients for the compression and tensile layers, respectively.(50) In this study it is assumed that all experimental materials are isotropic, allowing the simplification of the second rank tensor α_{ij} to single property value. The biaxial stresses associated with each layer were further calculated to be

$$\sigma_c = \varepsilon_r E_c' \left(1 + \frac{t_c E_c'}{t_t E_t'}\right)^{-1} \tag{2}$$

$$\sigma_t = -\sigma_c \frac{t_c}{t_t} \tag{3}$$

$$E_i' = E_i/(1 - v_i) \tag{4}$$

where σ_c and σ_t are the residual biaxial stresses associated with the compressive and tensile layers, t_i refers to the thicknesses of the tensile and compressive layers, and E_i is the Young's modulus of either layer. Lange goes further to state that due to the relations in Equations 2 and 3 above, a thin compressive layer ($t_c/t_t \rightarrow 0$) is desired to maximize the surface compressive stress and minimize tensile stress in the bulk.(9)

Threshold strength ceramics have been shown to reduce the effectiveness of two different types of cracks, the first of which is the surface crack. In ceramics and other brittle materials, the fracture toughness, K_C, is determined by calculating a stress intensity factor, K, in mode I failure (tensile). This stress intensity factor describes the increased stress field just ahead of a crack relative to the stress observed in the material's bulk. K is defined as

$$K = Y\sigma\sqrt{\pi a} \tag{5}$$

where σ is the applied stress, a is the sub-critical crack length, and Y is a dimensionless constant dependent on the geometry of the crack. Once the crack reaches a critical size, c, brittle failure occurs and the yield stress of the material, σ_c, has been reached. Equation 6 changes to

$$K_{IC} = Y\sigma_C\sqrt{\pi c} \tag{6}$$

when this critical condition is met. One means of increasing the fracture toughness of a brittle material is to reduce the initial flaw size, thereby requiring more stress in order to grow that flaw to critical size. Due to the compressive residual stress observed on the surface of threshold strength ceramics, the surface flaws are placed in compression. The surface flaws are forced shut due to the compressive stress, leading to an increase in fracture toughness.(3)

Additionally, the residual compressive stress acts to arrest cracks that begin below the surface. With ceramic materials, relatively large flaws can form within the bulk material due to accidental addition of organic materials during the processing steps. Things like clothing fibers and human hairs can find their way into the batching, mixing, and/or forming processes and burn out during the sintering stage to leave closed pores. Lange et al. have derived an equation that calculates the stress intensity factor of a crack that is found in the bulk tensile layer that extends outwards to the compressive layers.

$$K = \sigma_a(\pi a)^{1/2} + \sigma_c(\pi a)^{1/2}\left[\left(1+\frac{t_c}{t_t}\right)\frac{2}{\pi}\sin^{-1}\left(\frac{t_t}{2a}\right) - 1\right] \tag{7}$$

where σ_a is the applied stress, σ_c is the residual compressive stress, and a is half the crack length. With the compressive stress being negative, it is shown that in order for K to be greater than zero that the structure must have a large enough applied stress that the first term in Equation 7 above becomes greater than the compressive stress term. When one sets $2a = t_t + 2t_c$ and $K = K_{IC}$, Equation 7 above can be rearranged to an expression for threshold strength, σ_{thr}.(7)

$$\sigma_{thr} = \frac{K_c}{\left[\pi\frac{t_t}{2}\left(1+\frac{2t_c}{t_t}\right)\right]^{1/2}} + \sigma_c\left[1-\left(1+\frac{t_c}{t_t}\right)\frac{2}{\pi}\sin^{-1}\left(\frac{1}{1+\frac{2t_c}{t_t}}\right)\right] \qquad (8)$$

Because the core of threshold strength materials is in slight tension, these interior cracks are more prone to growth. When these cracks are in the interior with a length shorter than that of the core thickness ($2a \leq t_t$), they are influenced by the residual tensile stress, σ_t. As the crack grows due to either σ_t or a combination of applied stress and residual tensile stress ($\sigma_t + \sigma_a$) and begins to interact with the compressive layers ($t_t \leq 2a \leq t_t + 2t_c$), the crack tip experiences a decrease in stress intensity due to the residual compressive stress, σ_c. It is at this point that an external applied stress must be imparted upon the laminate in order to overcome the residual compressive stress and grow the crack to the critical length ($2a = t_t + 2t_c$). Figure 7 below provides a visual representation of these conditions that Lange used to derive threshold strength seen in Equation 8.

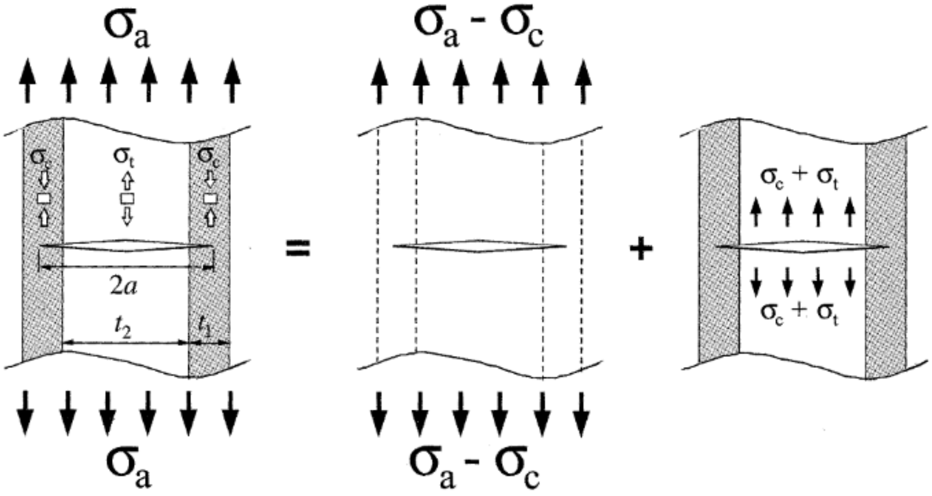

Figure 7: Stress fields used to calculate stress intensity factor of threshold strength ceramic laminate.(9)

The surface compressive layer also comes with some added benefits that further reduce the likelihood of unexpected catastrophic failure, the first of which is crack arrest. When a crack tip is within the thickness of the compressive stress region (whether that be an interior crack or surface crack), the compressive stress acts upon the flaw to close it arresting further growth.(4) In the case of an interior crack, once the crack grows to a length of $2a = t_t$ and begins interacting with the compressive layer, the residual compression acts to close off the tip, reduce stress intensity, and prevent further growth under the current stress state.(50) Unless the stress state is changed to have a tensile load great enough to overcome σ_c, the crack will not grow further into the compressive layer.

It was also found by the Lange group that a surface compressive layer can cause an interior crack to bifurcate upon interaction with the compressive layer.(51, 52) It was shown that with multiple ceramic material laminate combinations, including alumina and zirconia, crack bifurcation can occur when a crack tip extends into the compressive layer. Crack bifurcation is a process in which a crack tip slits into multiple cracks as it is growing, each possessing a fraction of the energy of the original crack. Bifurcation is a phenomenon that causes an overall decrease in crack energy and generally discourages catastrophic failure in ceramics. With each branch and changing of direction, the critical flaw loses energy, requiring a larger σ_a to reach failure.(52) Figure 8 below is an optical micrograph depicting the discussed bifurcation phenomenon on a Vickers indented four-point-bend coupon, where t_1 and t_2 coincide with the compressive and tensile layers, respectively.

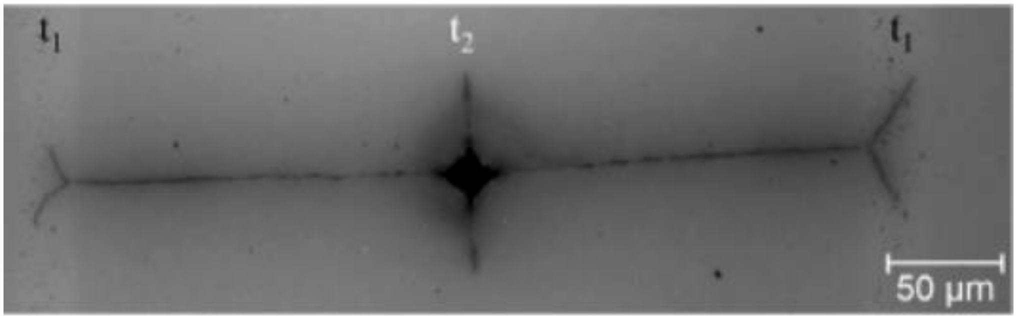

Figure 8: Optical micrograph showing interior crack bifurcation upon interaction with the compressive layer.(52)

1.3.4 Weibull Statistics

Weibull theory is commonly used to analyze the failure reliability of brittle materials. This statistical analysis method relates brittle failure to flaw density for a given material. The theory states a material with volume V is divided into n individual elements, ∂V, who are all under a tensile stress, σ. It is assumed that when one of these elements fails, the entire material fails, this is referred to as the weakest link assumption. At the given stress, σ, there is a probability of failure defined for each individual element, $P_f = f(\sigma, \partial V)$ with a probability of survival equal to $P_s = 1 - P_f$. The probability that a part contains a critical flaw increases with both part volume and applied stress. This model is further used to derive expressions for P_s and P_f of a ceramic material

$$P_s = exp\left(-V\frac{\sigma-\sigma_{thr}}{\sigma_o}\right)^m \tag{9}$$

$$P_f = 1 - exp\left(-V\frac{\sigma-\sigma_{thr}}{\sigma_o}\right)^m \tag{10}$$

where σ is the stress at failure, σ_{thr} is the threshold stress, σ_o is the characteristic strength (strength where failure probability is 63.2%), and m is the Weibull modulus. It should be noted that in most cases involving ceramics it is assumed that there is no stress under which failure probability is zero ($\sigma_{thr} = 0$). Additionally, volume is assumed to remain constant across all test samples, further simplifying Equation 9 to

$$P_s = exp\left(-\frac{\sigma-\sigma_{thr}}{\sigma_o}\right)^m \tag{11}$$

In order to conduct Weibull analysis of a material, fracture data must be collected. The least squares fit of this data is then taken to find the Weibull parameters, σ_o and m. This is accomplished by taking the natural logarithm twice of Equation 11 above, which is

$$\ln\ln\left(\frac{1}{1-P_f}\right) = m\ln(\sigma - \sigma_{thr}) - m\ln(\sigma_o) \tag{12}$$

By doing a linear fit to $\ln\ln\left(\frac{1}{1-P_f}\right)$ as a function of $\ln(\sigma)$, one can determine the Weibull modulus to be the slope of this line, while the normalizing stress is related to the $\ln\ln\left(\frac{1}{1-P_f}\right)$ intercept at $\ln(\sigma) = 0$. An example of this plot can be seen in Figure 9 below.

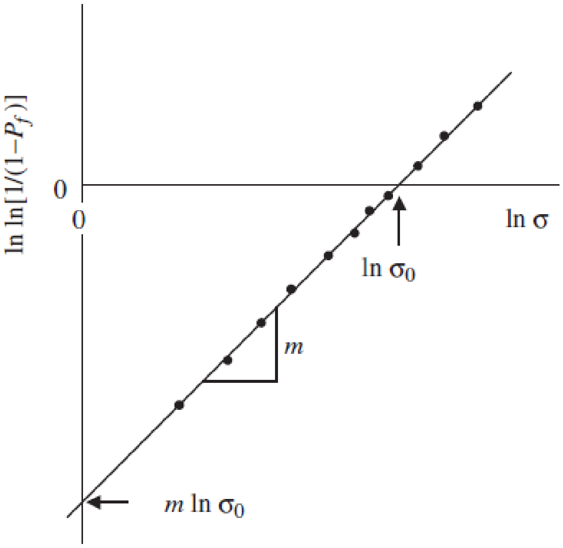

Figure 9: Weibull plot showing relationship between linear regression and Weibull parameters (Figure 7.2 in Wachtman).[53]

1.4 Objectives

The objectives of this proposed research are to: (i) create an all-ceramic dental prosthetic material that exhibits a threshold strength by 3D printing of alumina strengthened zirconia (ASZ) and zirconia (ZrO_2) to impart a surface compressive residual stress in originating from a CTE mismatch. (ii) quantify the residual stresses exhibited by the ASZ/ZrO_2 functionally graded material and estimate a threshold stress based on standard K_c values. (iii) produce a new 3D functionally graded material that exhibits greater mechanical performance and failure reliability than the ceramic materials currently being used in dental prosthetics.

2. METHODOLOGY

2.1 Ink Formulation

Ceramic inks are created by dispersing ceramic powder in an aqueous solution and then adding a counter polyelectrolyte to gel the ink until the desired rheology is achieved. The inks are formulated using the materials listed in **Table I** below. A solids loading of 43 percent by volume (ϕ_{solids}=0.43) is used in all inks as it is the maximum solids loading that produced a consistently printable ink. The formulations for 35mL batches of each ink can be found in **Table II**. Inks are batched in Thinky cups (see Figure 10) and mixed in a Thinky AR-250.

Table I. Ink Batching Materials

Material	Alias	Source	Purity	Notes
TZ-3YS-E zirconia powder	ZrO_2	Tosoh, Inc.	3wt% Y_2O_3	0.04μm avg particle size
AKP-30 alumina powder	Al_2O_3	Sumitomo Chemical Advanced Technologies	99.99%	0.27μm avg. particle size
Darvan 821A ammonium polyacrylate	D-821A	R.T. Vanderbilt Company, Inc.	40wt% Aq. Soln	Dispersant, MW 3500
Polyethyleneimine	PEI	MP Biomedicals, LLC	5wt% Aq. Soln.	Flocculant, MW 50,000-100,000
METHOCEL F4M Hydroxypropyl methylcellulose	F4M	The Dow Chemical Company	5wt% Aq. Soln.	Viscosifier solution

Table II. Calculated Ink Batches

Ink (ϕ = 0.43)	Solids, g	Dispersant, g	Viscosifier Solution, g	Flocculant, g	DI Water, g
Zirconia	91.053	0.615	3.990	0.125	15.145
Alumina	56.448	0.401	3.990	0.200	15.359

The batching process begins with enough 2.5mm diameter zirconia milling media to cover the bottom of a Thinky cup (~21g). The DI water and dispersant are weighed and added before mixing for 15 seconds to ensure homogenous distribution of the dispersant. Next, approximately 2/3 of the ceramic powder is added and mixed for 1 minute and 30 seconds, followed by the addition of the rest of the powder with another 1 minute and 30 seconds of mixing time. Adding the powders in two separate batches prevents large agglomerates from forming. With the ceramic powder dispersed, methocel F4M is added to increase the viscosity of the slurry, followed by 1 minute of mixing. Finally, PEI is gradually added and mixed for 30 seconds after each addition until the resting rheology is sufficient to form stiff peaks (see Figure 10). The ASZ ink used in this study is created by mixing both zirconia and alumina inks in a ratio of 20wt% Al_2O_3 to 80wt% ZrO_2 to form a 35mL mixture. This mixture ratio was calculated assuming both inks have the same solids loading $(\phi_{ZrO_2} = \phi_{Al_2O_3} = 0.43)$ and a batch size (V_t) of 35mL. The total weight of ceramic (m_{cer}) was calculated using

$$m_{cer} = V_t \phi \cdot \langle \rho \rangle = \frac{V_t \phi \left(\rho_A \bullet \rho_Z \right)}{(0.2\rho_Z + 0.8\rho_A)} \tag{13}$$

where ρ_i corresponds to the densities of the constituents. Knowing m_{cer}, the masses of each constituent (m_a and m_z) were calculated by multiplying m_{cer} by each constituent's respective weight percentage. Finally, the 35mL batch formulas from **Table II** were multiplied by a factor of $m_i / V_t \phi \rho_i$ and all components summed to find the weights of each ink needed to make the 80/20 ASZ ink.

Figure 10. Images of Thinky Cups used to batch ceramic inks. Image (right) of alumina ink showcasing stiff peaks.

2.2 Rheometry

The rheology of alumina, zirconia, and ASZ inks is measured using a Bohlin C-VOR 200 Rheometer (see Figure 11) with a C14 serrated bob. Both viscometry and oscillatory rheometry measurements are conducted using a 3.6mL sample from each ink. Viscometry measures shear stress (τ) and apparent viscosity (η) of the inks as a function of shear rate ($\dot{\gamma}$) using a shear rate range of $0.002 \leq \dot{\gamma} \leq 1500$ s^{-1}. Oscillation viscometry is used to measure the viscous (G'') and elastic (G') shear modulus of the inks as a function of τ. The rheometer was operated in controlled stress mode such that the appropriate τ range for observing yielding behavior in oscillatory mode depends on the specific ink.

Figure 11: Bohlin C-VOR 200 Rheometer and C14 serrated bob used in rheological measurements.

2.3 Robocasting

Prior to printing, a set of G-code has to be created to communicate the print instructions to the Robocaster (Figure 13). This is accomplished using the Lattice Builder feature in the RoboCAD software. In accordance with ISO 6872/2008 (biaxial flexure testing method for dental ceramics), a sample geometry resembling a cylindrical disk with a final diameter of $\varnothing$13.5mm and thickness of h=1.4mm is used in this study. The print model is enlarged to account for an estimated 30% linear shrinkage during sintering. A pitch (center-to-center spacing between adjacent printed lines) of p=0.330mm a layer height of δz=0.260mm is used with a deposition nozzle diameter of d_{tip}=0.33mm. Typically, $\delta_z=0.25\cdot\pi\cdot d_{tip}$ when $p=d_{tip}$ for space filling when the volumetric flow rate of ink is set to $q=0.25\cdot\boldsymbol{v}\cdot\pi\cdot d_{tip}^2$, where $\boldsymbol{v}$ is the vector speed of printing in the x-y plane. The 3D models of the biaxial flexure samples can be found in Figure 12 below.

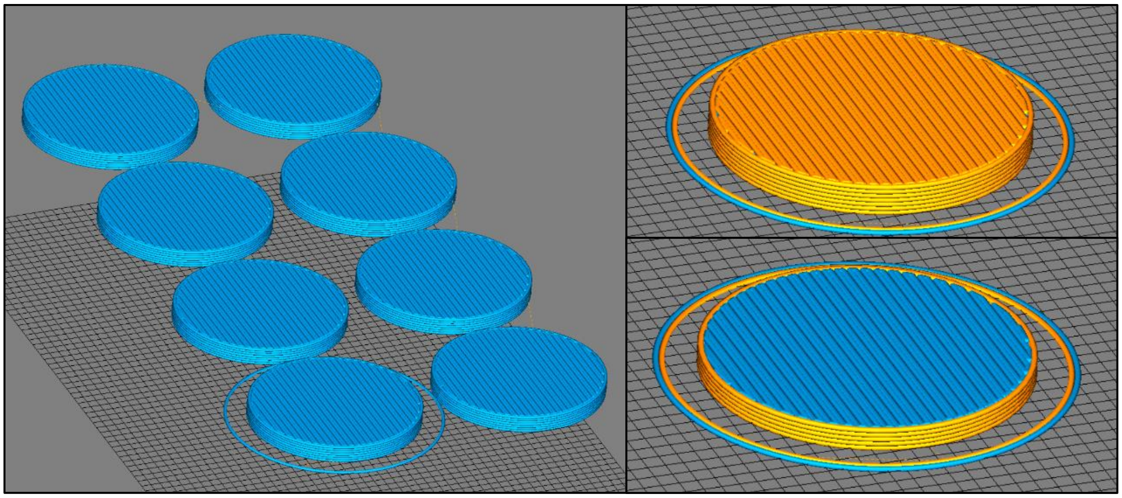

Figure 12: Models of single material (left) and multi-material (right) biaxial flexure disks.

The inks are carefully loaded into syringes, taking measures to eliminate all bubbles during the transfer, and connected to the deposition tip/nozzle via a 28cm long piece of tubing (see Figure 14). These syringes are then mounted in the Robocaster (see Figure 15) and connected to one of three actuators used to control extrusion. The ink is printed onto alumina substrates submerged in a lamp oil bath that prevented uneven drying during the printing process. Sample sets of 30 biaxial flexure disks are printed for each material system. The samples were then carefully removed from the bath and dried for 2 days in a fume hood. After drying, the green samples were subjected to a sintering cycle seen in Figure 16. Finally, a Micromeritics AccuPyc II 1340 Gas Pycnometer was used to measure sample densities to ensure proper sintering.

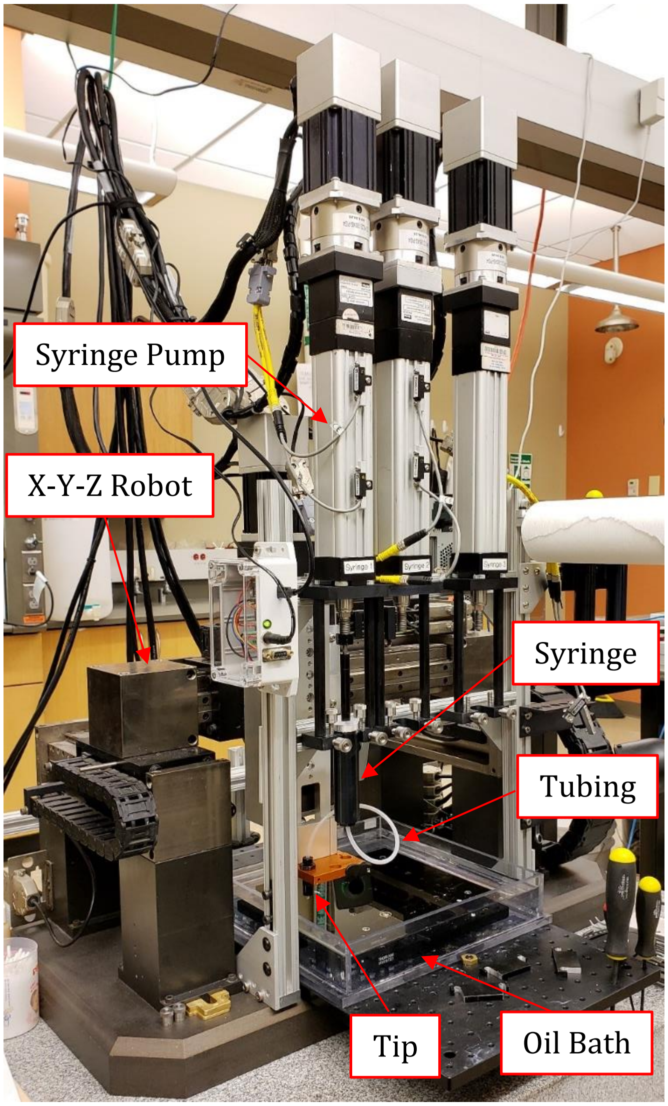

Figure 13: The Smay Group Robocaster.

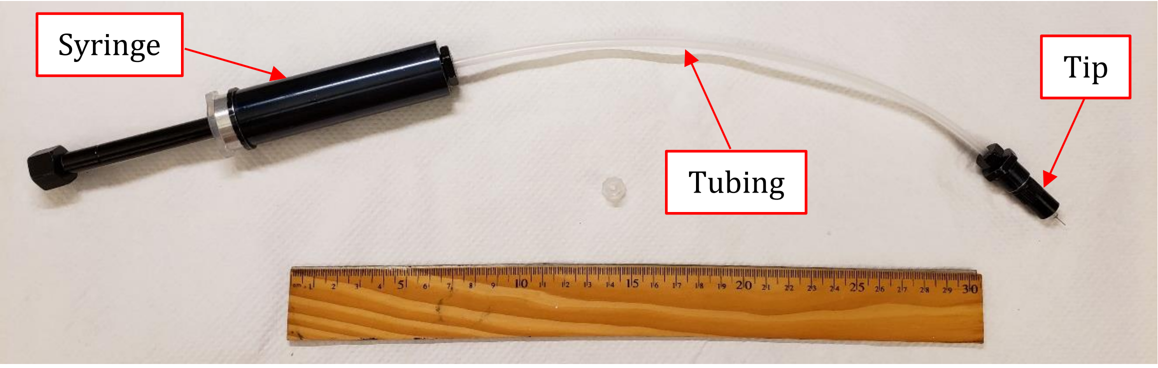

Figure 14: Ink syringe assembly.

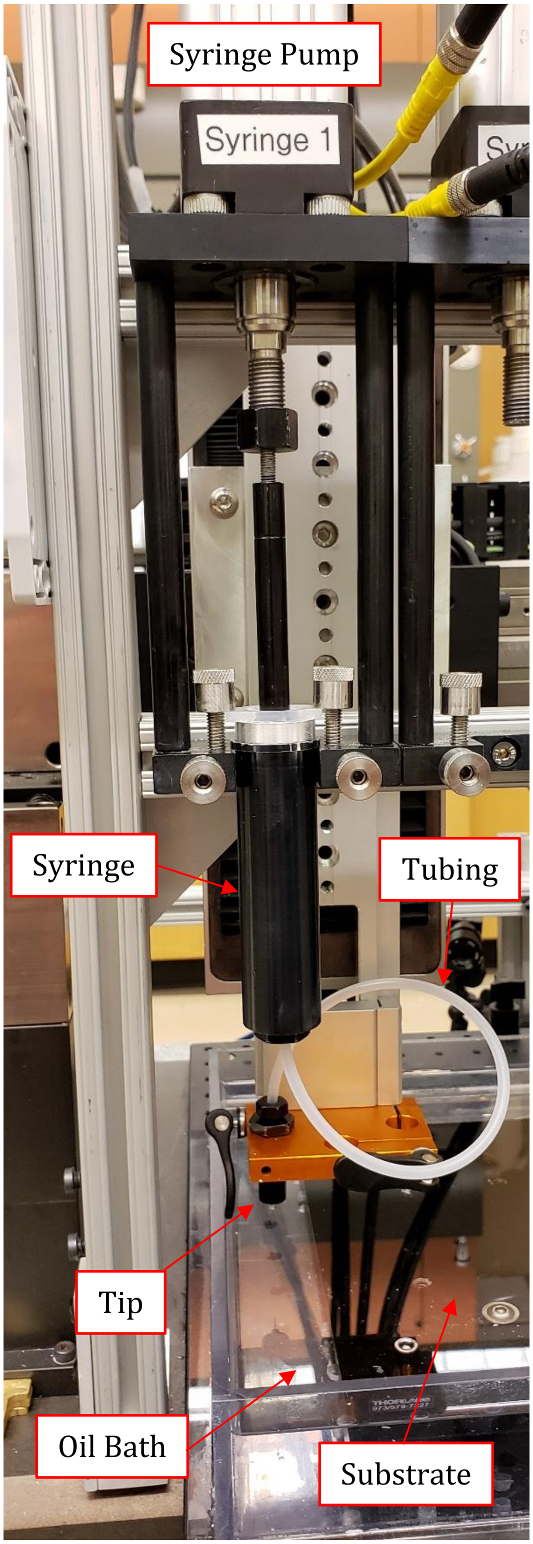

Figure 15: Syringe mounted in Robocaster.

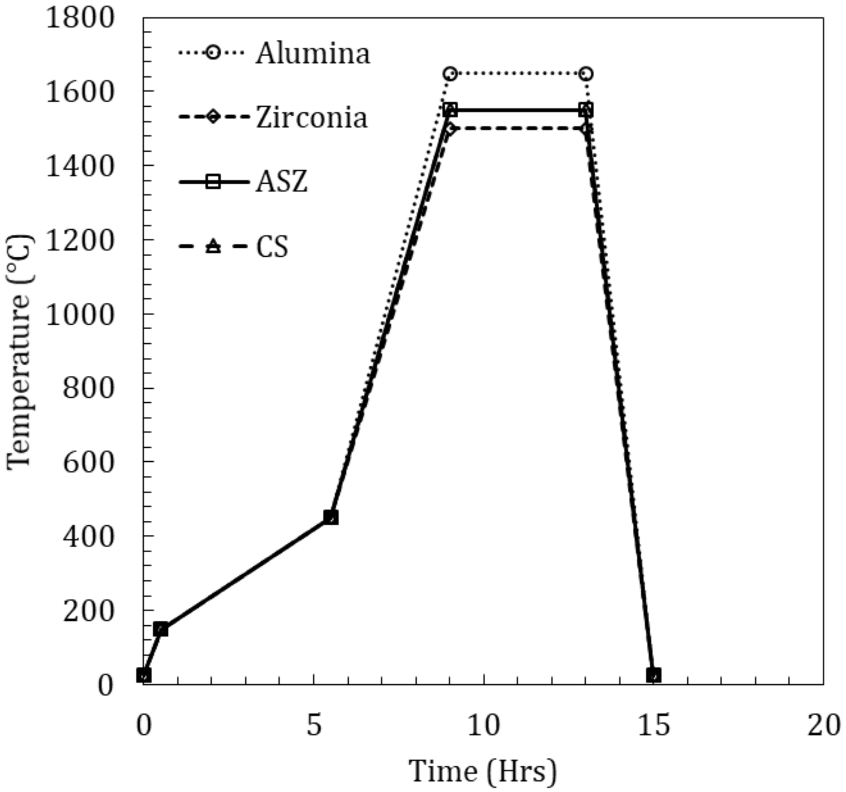

Figure 16: Sintering cycles for biaxial flexure test coupons.

2.4 Biaxial Flexure Testing

Once the samples are cooled, they are numbered and then measured with a micrometer (**Table AI through AIV in Appendix**). A 1cm X 1cm square of Teflon tape is stuck to each side of the disks which serves to keep the individual samples together after high-energy fracture. This tape is assumed to have a negligible effect on the observed flexural strength. A randomized test order list is generated in Excel for each material set to ensure statistical integrity.

The biaxial flexure disks are tested in a piston-on-three-ball fixture designed and machined for this experiment in accordance with ISO 6872/2008. The fixture is attached to the Robocaster in the configuration shown in Figures 17 and 18. One of the Robocaster actuators is used to apply load and measured using a CALT DYLY-103 100kg load cell. A co-axial locator hole is machined into the base and used for aligning the piston. The samples are tested using a constant displacement rate of 0.5 mm/min until failure, at which point the tests are ended and the failure load was recorded in grams. This failure load, P, is converted to newtons and used to calculate the failure stress of each sample, σ, using

$$\sigma = \frac{-0.2387\, P\, (X-Y)}{d^2} \tag{14}$$

$$X = (1+v)\ln\left(\frac{B}{C}\right)^2 + \left[\frac{1-v}{2}\right]\left(\frac{B}{C}\right)^2 \tag{15}$$

$$Y = (1+v)\left[1 + ln\left(\frac{A}{C}\right)^2\right] + (1-v)\left(\frac{A}{C}\right)^2 \tag{16}$$

where h is the disk thickness in mm, v is Poison's ratio, A is the support ball radius, B is the piston radius, and C is the specimen radius.

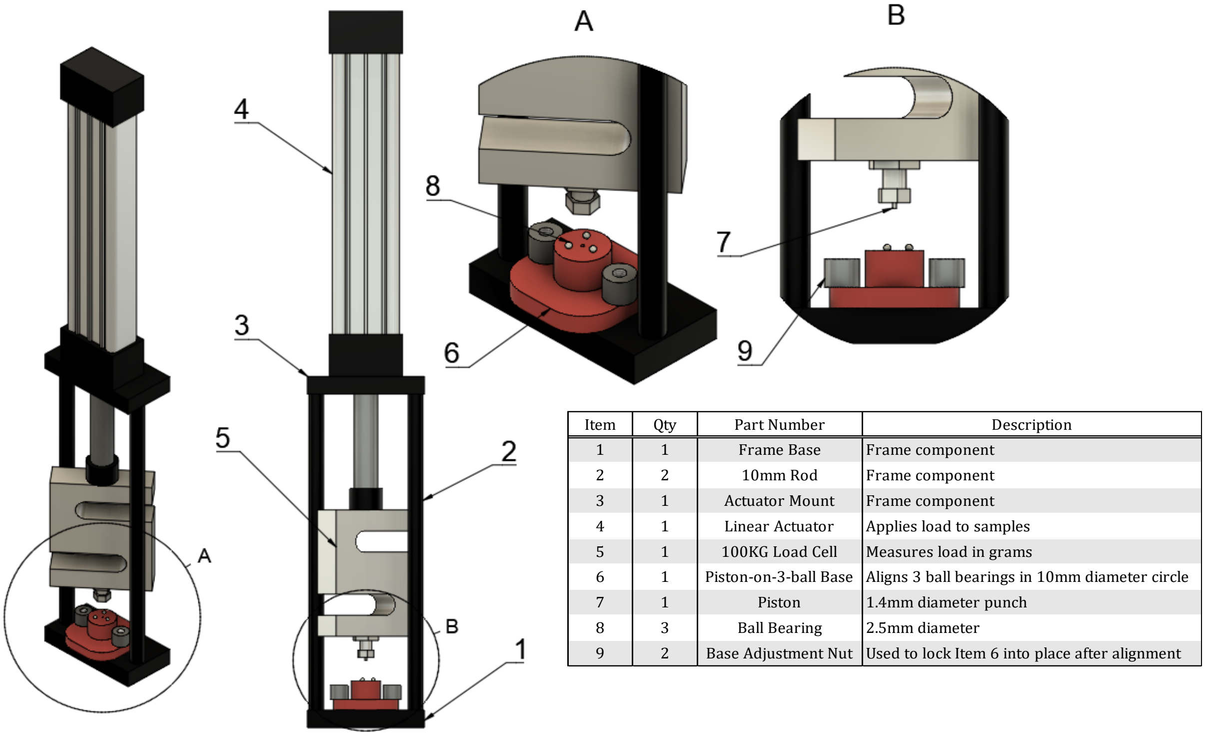

Item	Qty	Part Number	Description
1	1	Frame Base	Frame component
2	2	10mm Rod	Frame component
3	1	Actuator Mount	Frame component
4	1	Linear Actuator	Applies load to samples
5	1	100KG Load Cell	Measures load in grams
6	1	Piston-on-3-ball Base	Aligns 3 ball bearings in 10mm diameter circle
7	1	Piston	1.4mm diameter punch
8	3	Ball Bearing	2.5mm diameter
9	2	Base Adjustment Nut	Used to lock Item 6 into place after alignment

Figure 17: Schematic of Piston-on-Three-Ball Biaxial Flexure Fixture with items list.

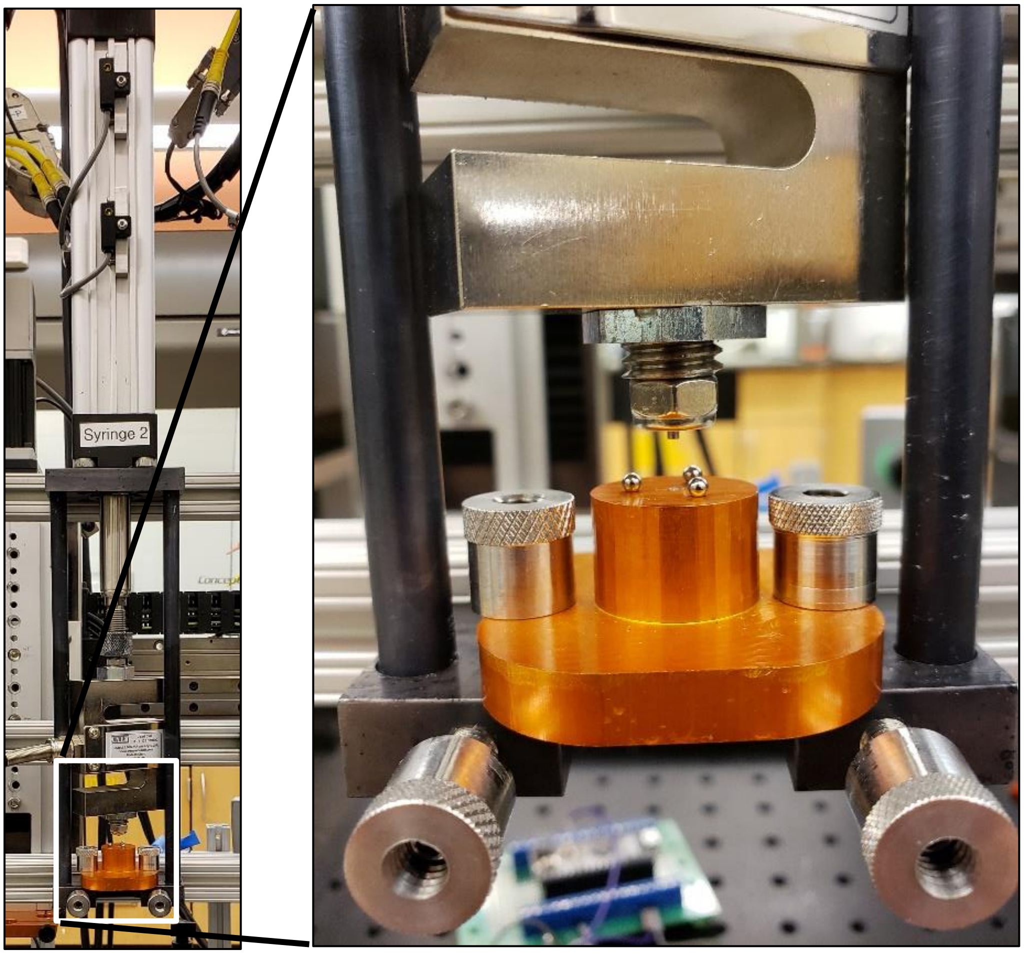

Figure 18: Piston-on-Three-Ball Biaxial Flexure Fixture designed and used for this experiment.

2.5 Weibull Analysis

Weibull analysis was conducted on all material sample sets to provide a metric of determining failure reliability. The sets of n samples were first ranked in ascending order (1 to n) based on failure stress where 1 is the rank of the sample with lowest failure stress and n is the highest. From the assigned numerical rank (i) a survival probability (P_s) was calculated.

$$P_s = 1 - \frac{i-0.5}{n} \tag{17}$$

$\ln\ln(P_S^{-1})$ was then plotted verses the natural log of the collected strength data for each material set. A linear trend line corresponding to Equation 12 was fit to each plot. As previously shown in Figure 9, the slope of this line is the Weibull modulus, m. Additionally, the normalizing stress, σ_0, was calculated by manipulating the Y-intercept of the trend line, which is equal to $m \ln(\sigma_0)$.

Unlike the other monolithic ceramics tested, the CS samples needed to take into account the estimated threshold stress when plotting to find m and σ_0 (refer back to Equation 12). To do this, the CS dataset was plotted as $\ln\ln(P_S^{-1})$ vs $\ln(\sigma^*)$ where

$$\sigma^* = \sigma - \sigma_{thr} \tag{18}$$

Additionally, any samples that did not fit the linear trend line were removed under the assumption that these samples failed at uncharacteristically low stresses due to abnormally large defects.

2.6 Determination of Residual and Threshold Stresses

In order to calculate the residual compressive, tensile and threshold stresses of the candy shell (CS) material, some material properties need to be determined. As shown previously in Equations 1, 2 and 8, σ_c and σ_{thr} are functions of α_t, α_c, E_t, E_c, ν_t, and ν_c. Using average isotropic properties for polycrystalline ceramics referenced from literature$^{(9)}$ for both ZrO_2 and Al_2O_3, α, E, and ν are calculated for ASZ using a volume fraction weighted average.

$$x_{ASZ} = \phi_{ZrO_2} x_{ZrO_2} + \phi_{Al_2O_3} x_{Al_2O_3} \tag{19}$$

where x_i is any of the previously stated material properties (α, E, or ν) for the corresponding constituents. The Poisson's ratio for the CS samples was also calculated using Equation 19.

However, the Young's modulus of these samples was calculated using the Ravichandran(54) estimate for two-phase systems

$$E = \frac{(cE_1E_2+E_2^2)(1+c)^2 - E_2^2 + E_1E_2}{(cE_1+E_2)(1+c)^2} \tag{20}$$

$$c = \left(\frac{1}{\phi_1}\right)^{1/3} - 1 \tag{21}$$

where $E_1$is the Young's modulus of the minor phase, E_2 is the Young's modulus of the major phase, *c* is a dimensionless parameter, and ϕ_1 is the volume fraction of the minor phase. The summation of these material properties can be seen in **Table III**.

Table III. Material Properties of Experimental Ceramics

Material	ν	α/<α> ($x10^{-6}$ °C^{-1})	E /<E> (GPa)
Zirconia	0.310	11.35	205
Alumina	0.250	8.30	401
ASZ (ϕ_{Al2O3} =0.723)	0.293	10.51	244
CS (ϕ_{ASZ} =0.338)	0.304	N/A	218

Having determined these material properties, the estimated σ_c and σ_t are calculated using Equations 1 through 4. A compressive layer thickness of t_c = 0.4 mm and a tensile layer thickness of t_t = 1 mm is used to calculate these values. These dimensions are based on the RoboCAD model used to print the biaxial flexure samples adjusted for sintering shrinkage to the ISO 6872/2008 standards. Equation 8 is used to calculate an estimated σ_{thr} of the CS samples. This estimate is based on a lower bound typical fracture toughness for commercial ceramics of K=5 MPa$\sqrt{m}$.(53) Unfortunately, the actual fracture toughness of the samples was unable to be measured due to unforeseen circumstances. Aka COVID-19.

3. RESULTS

3.1 Ink Rheology

All three colloidal gel inks exhibit pseudoplastic with yield stress behavior under an imposed increasing τ sweep for $10^{-4} \leq \dot{\gamma} \leq 10^{3}$ s^{-1}. η_{app} as a function of $\dot{\gamma}$ is shown in Figure 19. A least squares fit of the viscometry data using the Herschel-Buckley rheological model

$$\tau = \tau_y + K\dot{\gamma}^n \tag{22}$$

reveals the shear thinning coefficients (n), yield stresses (τ_y), and enumerated in **Table IV**.

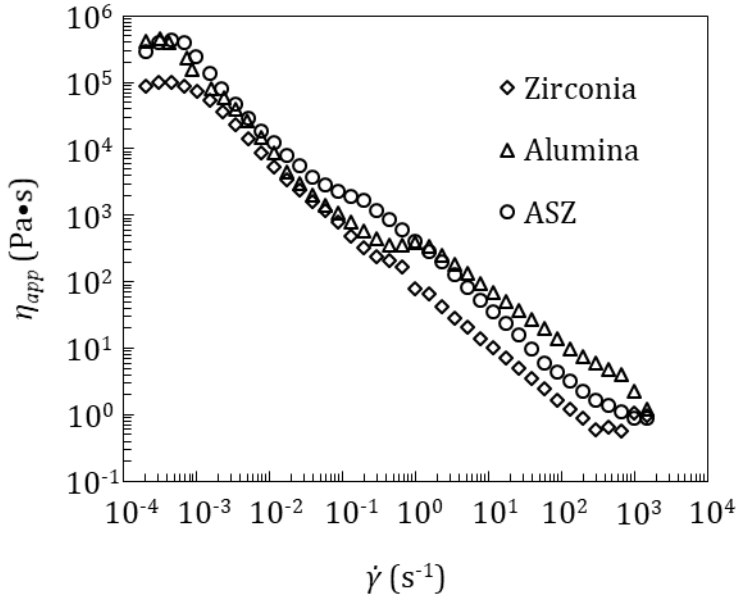

Figure 19: Apparent viscosity (η_{app}) as a function of shear rate ($\dot{\gamma}$) for ZrO_2, Al_2O_3 and ASZ colloidal gel inks.

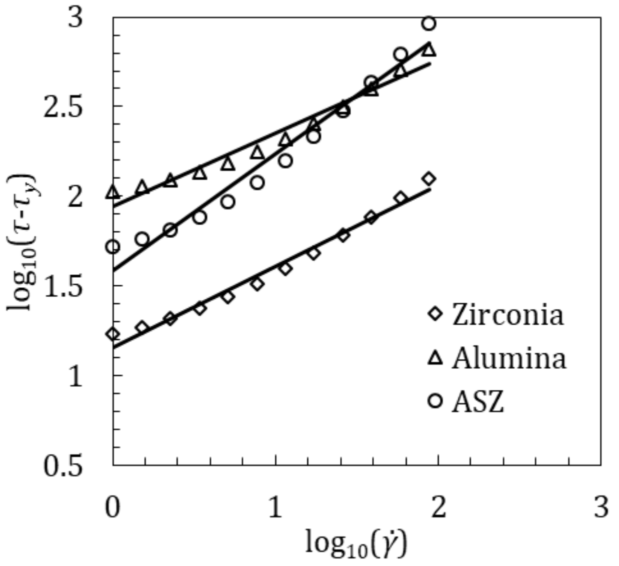

Figure 20: Linear plot of $\log_{10}(\tau\text{-}\tau_y)$ as a function of $\log_{10}(\dot{\gamma})$ for the three ceramic inks. Linear fits were used to determine Herschel-Bulkley viscosity parameter and shear thinning exponent.

Figure 21 shows elastic modulus (G') as a function of shear stress amplitude (τ) for oscillatory rheologic measurements. The inks show an identifiable equilibrium moduli (G'_{eq}) within their respective linear viscoelastic regions. Additionally, all inks exhibited a yield stress (τ_y) which was evaluated at $G' = 0.9G'_{eq}$.(40) These properties are summarized in **Table IV**.

Table IV. Summary of Rheological Properties

Ink	G'$_{eq}$ (Pa)	τ_y (Pa)	K (Pa•s^n)	n
Zirconia	4.27x10^3	7.8x10^1	0.06	0.57
Alumina	1.30x10^6	1.34x10^2	0.20	0.65
ASZ	1.79x10^3	1.57x10^2	0.29	0.41

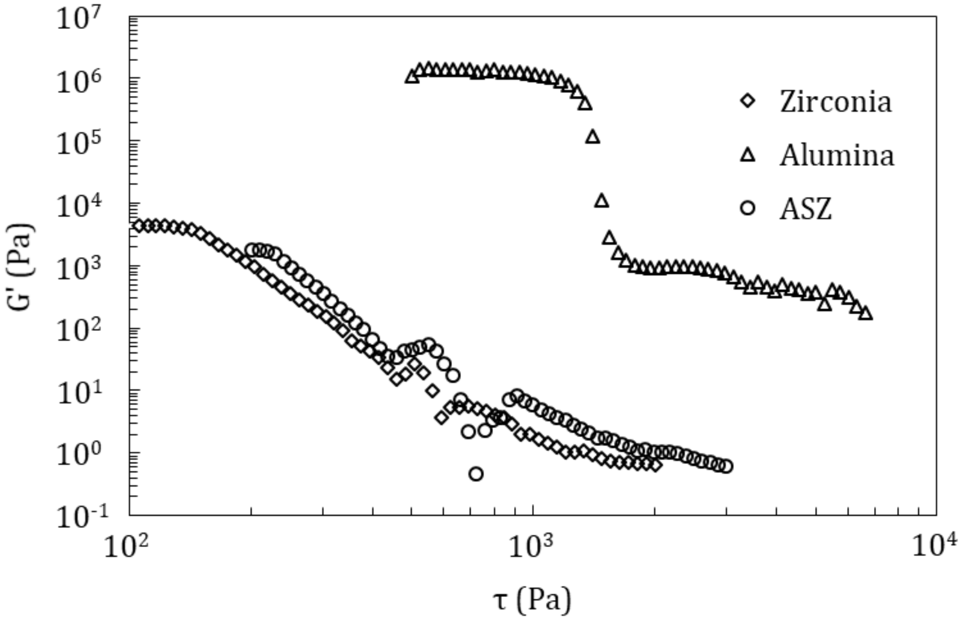

Figure 21: log-log plot of elastic modulus (G') as a function of increasing shear stress amplitude (τ) at 1 Hz for zirconia, alumina and ASZ colloidal inks.

3.2 Biaxial Flexure Testing and Weibull Analysis

Density measurements conducted on the flexural test samples confirm proper densification as shown in **Table V.** A collection of biaxial flexure strength data for each material set can be seen in Figure 22. It should be noted that the samples within the red box in Figure 22 were culled due to poor fit during Weibull analysis. The CS samples outperformed the other materials in both flexural strength and Weibull parameters. The materials ranged in average flexural strength by 418.1 MPa where the CS samples averaged the highest with 670.22 ± 69.74 MPa while alumina was the lowest with 252.12 ± 52.42 MPa. The CS samples possessed a Weibull modulus of 8.6 and characteristic stress of 737.15 MPa after the data culling. This shows a significant improvement in reliability over both of the CS constituent materials (zirconia and ASZ). Figure 23 shows the plots used to find the Weibull parameters for all four materials. A summary of the data collected from biaxial flexure testing and Weibull analysis can be found in **Table VI**.

Table V: Densification of Experimental Ceramic Materials

Material	Theoretial Density (g/cm^3)	Densification (%)
Zirconia	6.05	98.4
Alumina	3.95	98.3
ASZ (ϕ_{Al2O3} =0.723)	5.47	97.6
CS (ϕ_{ASZ} =0.338)	5.85	97.9

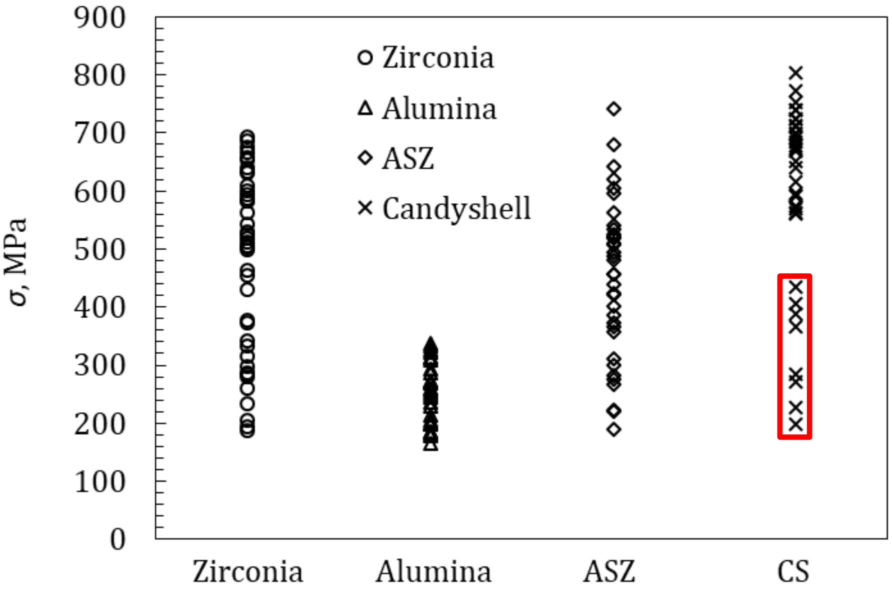

Figure 22: Biaxial flexure strengths of robocast dental ceramics.

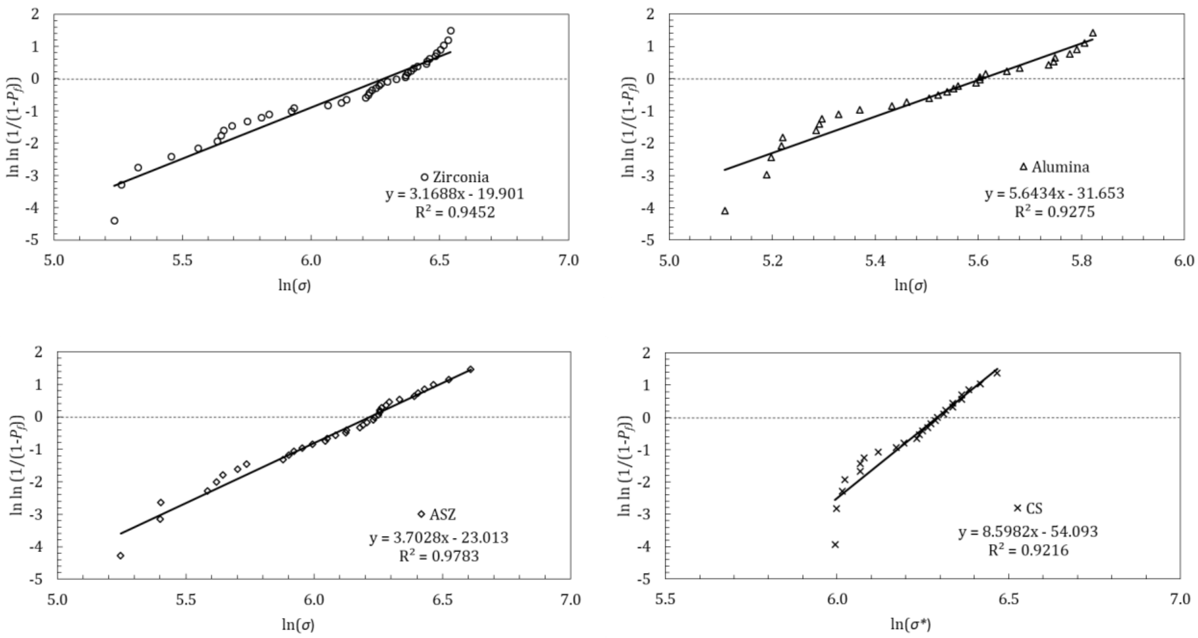

Figure 23: ln ln (1/(1-P_f)) vs ln (σ) plots for zirconia (upper left), alumina (upper right), and ASZ (bottom left). ln ln (1/(1-P_f)) vs ln (σ^*) plot for CS (bottom right).

Table VI: Summary of Biaxial Flexure Testing and Weibull Analysis

Material	σ_{avg}, MPa	σ_0, MPa	m
Zirconia	476.02 ± 156.89	441.84	3.17
Alumina	246.73 ± 52.42	272.83	5.64
ASZ	451.14 ± 135.90	500.21	3.70
CS	670.22 ± 69.74	737.15	8.60

3.3 Residual and Threshold Stresses

The residual thermal stresses calculated for the CS samples were found to be substantial. Using a thermal strain of -9.45x10^{-4} calculated from a cooling range of 1550°C to 25°C, the residual compressive and tensile stresses were found to be -227.79 MPa and 91.11

MPa, respectively. Additionally, the estimated threshold strength based on a fracture toughness lower bound of 5 MPa$\sqrt{m}$ was found to be 160.12 MPa.

3.4 Failed Experiments

3.4.1 Four-Point Bend Testing

Flexural strength and fracture toughness characterization was initially going to be conducted using a four-point bending (4pt-bend) test in configuration A outlined in ASTM C1161-18. Bars were printed to have a post-sintering geometry in accordance with configuration A: overall length (L_T of 25 mm, width (b) of 2 mm, and depth (d) of 1.5mm. A notch (1 mm width, 0.5 mm depth) was printed into each test bar for use as an initial flaw for calculation of $K_{C,4pt}$. The printed samples can be viewed in Figure 24. The fully articulating 4pt-bend fixture used for this experiment was designed and manufactured based on the ASTM diagram in Figure 25 and can be seen in Figure 26. The fixture was attached to the Robocaster similarly to that of the piston-on-3-ball fixture. The failure stresses obtained using this flexural strength test were an order of magnitude lower than the expected range. Additionally, only 2 fractures of the 120 tested samples occurred at the notch, preventing the calculation of fracture toughness. This lead the group to believe that the specimen geometry had large periodic flaws caused by the Robcaster's cornering limitations. Due to this, the test method was abandoned and replaced by piston-on-3-ball biaxial flexure testing.

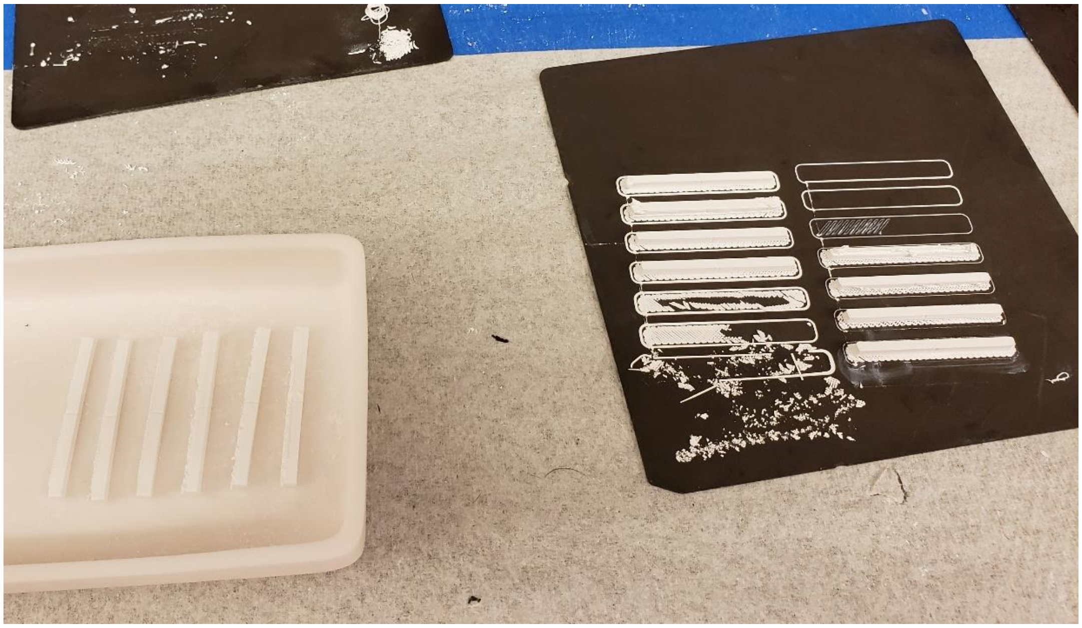

Fixture 24: Green body four-point bending test bars.

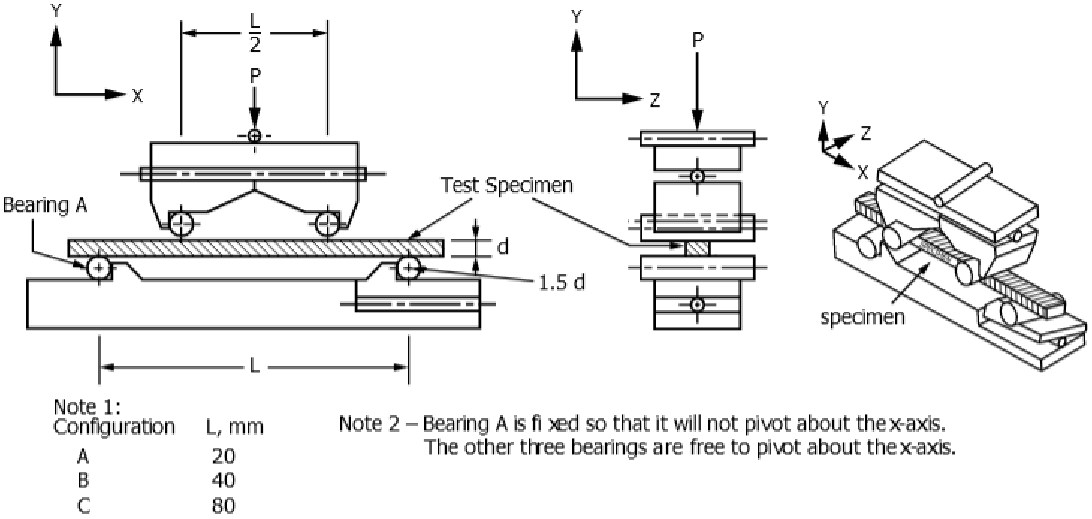

Figure 25: ASTM diagram of fully articulating four-point bending fixture.

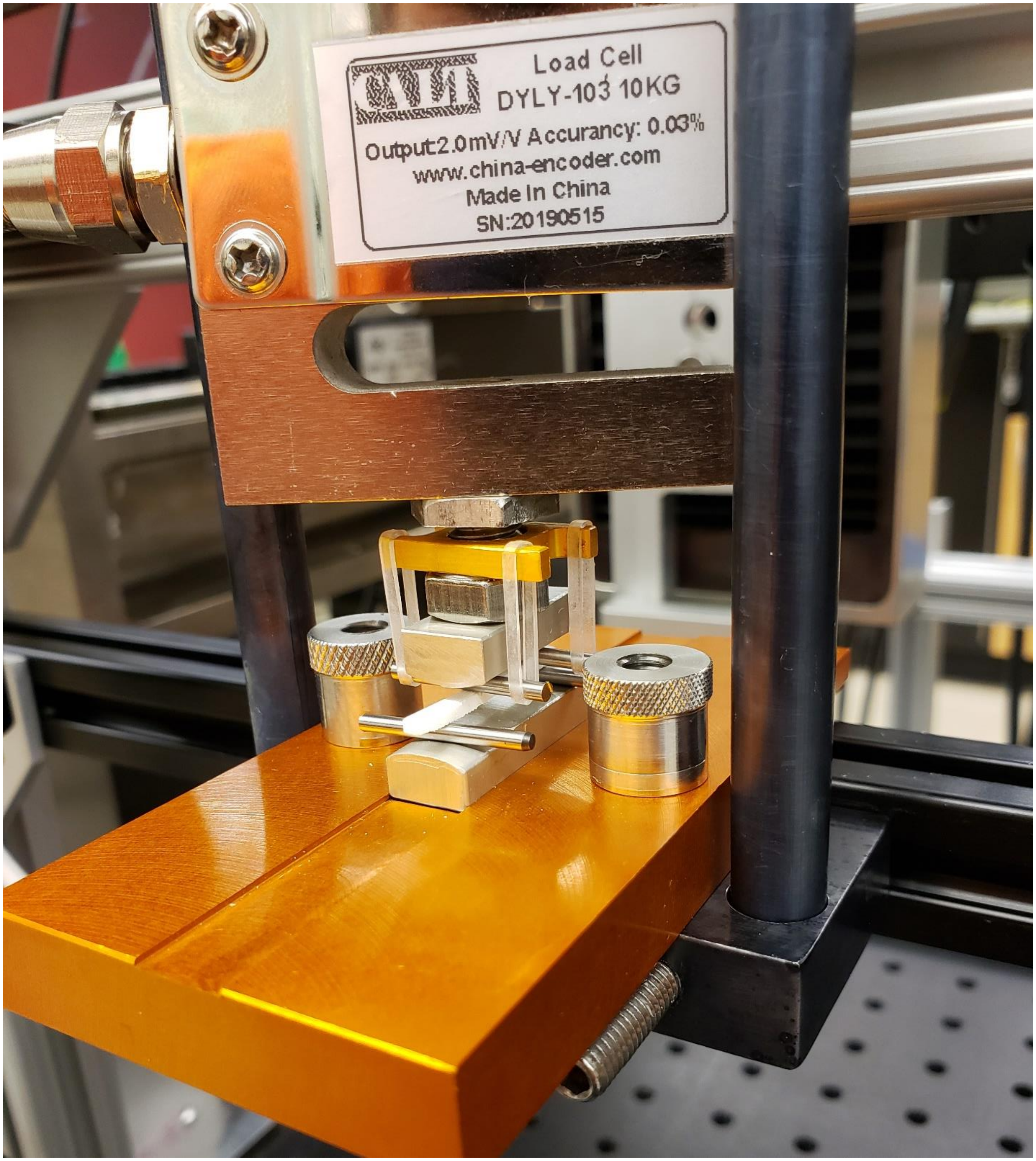

Figure 26: Fully articulated four-point bend fixture used in experiment.

3.4.2 Alumina Coated Zirconia Candy Shell

Originally, the project was intending to produce CS samples using an Al_2O_3 shell instead of ASZ. However, the residual stresses caused by the differential thermal strain were too great, resulting in fracture upon cooling. In the vast majority of samples, the contour ring of alumina had completely jettisoned and the main body fractured into two or more pieces. These failed samples can be seen in Figure 27. It was decided to move forward with a material that would produce a lower residual stress to ensure sample survival during sintering. ASZ with an 80/20 wt% ratio of ZrO_2/Al_2O_3 was selected due to it being a readily available material that is commonly used as a dental ceramic. These samples survived with a 100% success rate due to the significantly lower thermal strain.

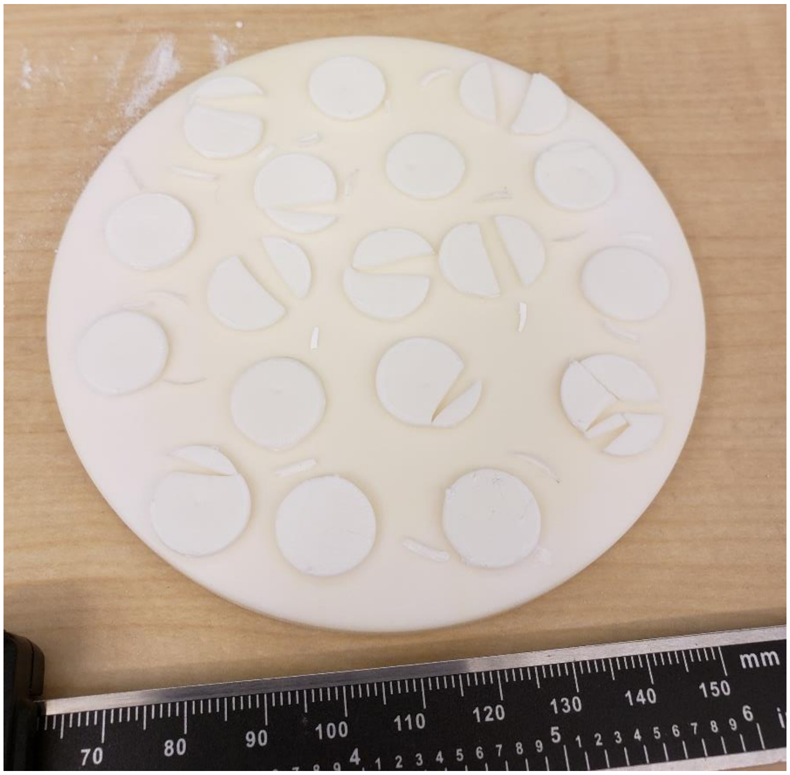

Figure 27: Alumina coated zirconia CS samples post-sintering.

4. DISCUSSION

4.1 Ink Rheology

The rheological properties of the inks used in this experiment were tested to ensure they would possess the proper flow characteristics for robocasting. All inks possessed the desired pseudoplastic yield behavior which was confirmed by fitting to the Herschel-Bulkley model. Figure 21 shows a major discrepancy between the Al_2O_3 ink and the ZrO_2 containing inks where the Al_2O_3 ink shows a much greater G' and τ_y. For this reason, the reported yield stresses in **Table IV** are derived solely from the Herschel-Bulkley model fit shown in Figure 20. This large discrepancy is most likely due to the difference in isoelectric point (IEP) between Al_2O_3 (pH 8-9) and ZrO_2 (pH 4-6). Because of the difference in IEP, the particles of these two materials interact with the dissociated dispersant (ammonium polyacrylate pH 7-8) by adsorbing differing degrees of the polyelectrolyte, affecting the strength of the formed gel network.

4.2 Mechanical Properties of Experimental Materials

It was found that the CS samples possessed the highest average strength and Weibull parameters out of the four materials tested in this experiment. It is likely that this overall improvement in mechanical performance is due to threshold strength. A collection of flexural strengths for commonly used dental ceramics gathered from a variety of flexural tests (ring-on-ring, piston-on-ring, piston-on-3-ball, and 3-point bending) was compiled by Rekow et al.(22, 23) and is shown in **Table VII** below. When comparing the flexural strength of the CS samples (670.22 ± 69.74 MPa) to other commonly used dental ceramics, it is apparent that it has greater flexural strength than all but the Pyrozyr and the upper bounds of Procera and InCeram Zirconia materials. It should be noted that Rekow explicitly reports the piston-on-3-ball flexural strength of Procera was 639.5 ± 115.8 MPa, which is slightly lower than the CS samples. The most promising comparison can be found between the CS material and the crown materials listed in **Table VII**. The ASZ/ZrO_2 CS material is intended to be applied as a new crown material and is showing a significantly larger flexural strength than that of the standard crown materials below.

Table VII: Dental Ceramics and Corresponding Mechanical Properties

Material Name	Type	Use	Flexural Strength, (Mpa)	Toughness, (MPa√m)
Dicor	Castable glass ceramic (Mica in glassy matrix)	Monolithic crown	114-120	1.2
Dicor-MGC	Machinable glass ceramic (Mica in glassy matrix)	Monolithic crown	216-230	1.2
IPS Empress	High leucite pressable porcelain	Monolithic crown	120-180	1.7
IPS Empress 2	Lithium disilicate reinforced pressable glass ceramic	Core	400	2.8-3.3
InCeram	Alumina infiltrated with glass	Core	450-600	4.5
InCeram Spinell	Spinell infiltrated with glass	Core	350-377	4.5
InCeram Zirconia	Zirconia infiltrated with glass	Core	600-800	4.5
Mark II	High leucite porcelain	Crown	122-140	1.8
OPC/ Optec	High leucite pressable porcelain	Crown	105-167	1.9
Procera	Slip cast alumina	Core	600-687	4.5
Prozyr	Zirconia infiltrated with glass	Core	833-1032	4.9

4.3 Future Work

This study has shown that the intentionally manufactured threshold stress in the CS samples has had a significant and positive effect on the material's flexural strength and reliability. However, this stress could be increased significantly by increasing the ratio of thermal expansion coefficients and layer thicknesses for the interior vs exterior layers. A greater difference between CTE's would result in a greater magnitude of thermal strain, leading to a higher compressive residual stress. As previously stated, the original plan for this study was to produce an Al_2O_3 coated ZrO_2 CS material instead of ASZ coated ZrO_2. However, the residual thermal stresses were too great, causing separation between the core and shell in the Al_2O_3/ZrO_2 system upon post-sintering cooling, resulting in sample destruction (see Figure 27). Due to the significantly lower differential thermal strain, the samples survived the sintering process but resulted in a much lower potential threshold strength. Future work should focus on grading the composition between a zirconia core and alumina shell to reduce the likelihood of separation between the two constituents.

Additionally, as previously stated in Chapter 1, the ideal scenario for threshold strength materials is to have a much thicker core than the compressive layer. As $t_c / t_t \rightarrow 0$, σ_c is maximized and $\sigma_t \rightarrow 0$. Unfortunately with a deposition nozzle diameter of 0.330 mm, the thinnest possible outer layer was ~0.200 mm, which is relatively thick compared to the layer thicknesses produced by the Lange group via slip casting.(9) Due to this, the ratio of core to coating material was far greater than the ratios reported by Lange and therefore resulted in lower threshold strength values. In the future, work should be done with alumina powder possessing a smaller particle size. This would allow for the use of smaller deposition nozzle diameters for the purpose of reducing the coating layer thickness.

5. CONCLUSION

In this study, a threshold strength dental ceramic consisting of a ZrO_2 core and ASZ coating was manufactured using direct ink writing. The threshold stress was induced via a thermal expansion differential between the two materials during post-sintering cooling. The threshold strength material, referred to as the candy shell material, was tested in biaxial flexure using the piston-on-3-ball method described in ISO 6872/2008 alongside monolithic samples of the three constituent materials (ZrO_2, Al_2O_3, and ASZ). It was found that the CS material possessed the greatest average flexural strength (670.22 ± 69.74 MPa) of the four materials tested, and possessed significantly greater flexural strength than several ceramics commonly used as crown materials. Additionally, Weibull analysis was performed to provide a quantifiable metric for failure reliability where the CS material outperformed the other tested materials in both Weibull modulus ($m = 8.60$) and characteristic strength ($\sigma_0 = 737.15$ MPa). In light of these results, functionally graded threshold strength ceramics produced via robocasting show great promise as potential dental ceramics.

Future work should focus in three areas: *i*) grading composition between core and shell materials in the robocasting process via an active mixer designed by Dr. Smay.(55, 56) This will hopefully reduce the chances of delamination between core and shell due to thermal strain, allowing for the use of materials with a greater thermal expansion differential. *ii*) using an alumina ink with smaller mean particle size to allow for printing with smaller tip diameters. This will reduce the minimum coating material thickness and reduce the ratio of t_c/t_t thereby further optimizing threshold strength. *iii*) performing supplementary mechanical testing to determine fracture toughness and fatigue resistance.

REFERENCES

1. Fair GE, He MY, McMeeking RM, Lange FF. Ceramic composites with three-dimensional architectures designed to produce a threshold strength - II. Mechanical observations. Journal of the American Ceramic Society. 2005;88(7):1879-85.
2. Lange FF, Rao MP, Hbaieb K, McMeeking RM. Ceramics that exhibit a threshold strength. Ceram Trans. 2002;134(Ceramic Armor Materials by Design):499-509.
3. Green DJ. Compressive surface strengthening of brittle materials. Journal of Materials Science. 1984;19(7):2165-71.
4. Green DJ, Tandon R, Sglavo VM. Crack Arrest and Multiple Cracking in Glass Through the Use of Designed Residual Stress Profiles. Science. 1999;283(5406):1295-7.
5. Moon H, Pontin MG, Lange FF. Crack interactions in laminar ceramics that exhibit a threshold strength. Journal of the American Ceramic Society. 2004;87(9):1694-700.
6. Pontin MG, Lange FF. Effects of porosity on the threshold strength of laminar ceramics. J Am Ceram Soc. 2005;88(2):376-82.
7. Rao MP, Lange FF. Factors affecting threshold strength in laminar ceramics containing thin compressive layers. J Am Ceram Soc. 2002;85(5):1222-8.
8. Honeyman-Colvin P, Lange FF. Infiltration of Porous Alumina Bodies with Solution Precursors: Strengthening via Compositional Grading, Grain Size Control, and Transformation Toughening. Journal of the American Ceramic Society. 1996;79(7):1810-4.
9. Rao MP, Sbnchez-Herencia AJ, Beltz GE, McMeeking RM, Lange FF. Laminar ceramics that exhibit a threshold strength. Science (Washington, D C). 1999;286(5437):102-5.

10. Pontin MG, Rao MP, Sanchez-Herencia AJ, Lange FF. Laminar ceramics utilizing the zirconia tetragonal-to-monoclinic phase transformation to obtain a threshold strength. J Am Ceram Soc. 2002;85(12):3041-8.
11. Rao MP, Rodel J, Lange FF. Residual stress induced R-curves in laminar ceramics that exhibit a threshold strength. J Am Ceram Soc. 2001;84(11):2722-4.
12. Moon H, Bahk J-H, Lange FF. Threshold strength and residual stress analysis of zirconia-alumina laminates. Int J Mater Res. 2007;98(8):674-81.
13. Cesarano J. A Review of Robocasting Technology. MRS Proceedings. 1998;542:133.
14. Huang M, Niu X, Shrotriya P, Thompson V, Rekow D, Soboyejo WO. Contact Damage of Dental Multilayers: Viscous Deformation and Fatigue Mechanisms. J Eng Mater Technol. 2005;127(1):33-9.
15. Huang M, Rahbar N, Wang R, Thompson V, Rekow D, Soboyejo WO. Bioinspired design of dental multilayers. Mater Sci Eng, A. 2007;A464(1-2):315-20.
16. Lawn BR, Pajares A, Zhang Y, Deng Y, Polack MA, Lloyd IK, et al. Materials design in the performance of all-ceramic crowns. Biomaterials. 2004;25(14):2885-92.
17. Malament KA, Natto ZS, Thompson V, Rekow D, Eckert S, Weber H-P. Ten-year survival of pressed, acid-etched e.max lithium disilicate monolithic and bilayered complete-coverage restorations: Performance and outcomes as a function of tooth position and age. J Prosthet Dent. 2019;121(5):782-90.
18. Malament KA, Socransky SS, Thompson V, Rekow D. Survival of glass-ceramic materials and involved clinical risk: variables affecting long-term survival. Pract Proced Aesthet Dent. 2003;Suppl:5-11.
19. Rekow D, Thompson VP. Near-surface damage--a persistent problem in crowns obtained by computer-aided design and manufacturing. Proc Inst Mech Eng H. 2005;219(4):233-43.
20. Rekow D, Thompson VP. Engineering long term clinical success of advanced ceramic prostheses. J Mater Sci: Mater Med. 2007;18(1):47-56.

21. Rekow D, Zhang Y, Thompson V. Can material properties predict survival of all-ceramic posterior crowns? Compend Contin Educ Dent. 2007;28(7):362-8; quiz 9, 86.
22. Rekow ED, Thompson VP. Clinical performance - A reflection of damage accumulation in ceramic dental crowns. Key Engineering Materials2001. p. 115-34.
23. Thompson VP, Rekow DE. Dental ceramics and the molar crown testing ground. J Appl Oral Sci. 2004;12(spe):26-36.
24. Willems E, Zhang F, Van Meerbeek B, Vleugels J. Iron oxide colouring of highly-translucent 3Y-TZP ceramics for dental restorations. J Eur Ceram Soc. 2019;39(2-3):499-507.
25. The challenge of the polygonal-to-BRep conversion [Image].
26. Zhu C, Smay JE. Rheology and flow behavior of concentrated colloidal gels for direct-write assembly of 3D mesoscale structures. Solid Freeform Fabr Symp Proc. 2010:634-45.
27. Zhu C, Smay JE. Shape evolution of spanning structures fabricated by direct-write assembly of concentrated colloidal gels. Ceram Trans. 2011;225(Processing and Properties of Advanced Ceramics and Composites III):131-43.
28. Smay JE, Lewis JA. Solid Free-Form Fabrication of 3-D Ceramic Structures. Ceramics and Composites Processing Methods2012. p. 459-84.
29. Bale H, Hanan JC, Smay JE. Thermal interface stresses including 3D microstructures in layered free-form ceramics. Ceram Eng Sci Proc. 2009;29(7, Advances in Bioceramics and Porous Ceramics):3-17.
30. Lewis JA, Smay JE, editors. Three-dimensional periodic structures2005: Wiley-VCH Verlag GmbH & Co. KGaA.
31. Witek L, Murriky A, Clark E, Smay J, Pines M, Silva N, et al. Mechanical, chemical, and in vivo characterization of biphasic HA/βTCP 3-D printed scaffolds for custom bone repair applications. Trans Annu Meet Soc Biomater. 2010;32(Annual Meeting of the Society for Biomaterials: Giving Life to a World of Materials, 2010, Volume 2):580.
32. Cai K, Roman-Manso B, Smay JE, Zhou J, Osendi MI, Belmonte M, et al. Geometrically complex silicon carbide structures fabricated by robocasting. J Am Ceram Soc. 2012;95(8):2660-6.

33. Lewis JA, Smay JE, Stuecker J, Cesarano J, III. Direct ink writing of three-dimensional ceramic structures. J Am Ceram Soc. 2006;89(12):3599-609.
34. Rahaman MN. Ceramic Processing. Boca Raton, FL: Taylor and Francis Group; 2007 2007.
35. Lewis JA. Colloidal processing of ceramics. J Am Ceram Soc. 2000;83(10):2341-59.
36. Jamal M. A. Alsharef MRT, Tanveer Ahmed Khan. Physical dispersion of nanocarbons in composites-a review. Universiti Teknologi Malaysia. 2016;79(5).
37. Benelmekki M. Introduction. 2019. In: Nanomaterials [Internet]. Morgan & Claypool Publishers; [1---14].
38. Lewis JA. Direct-write assembly of ceramics from colloidal inks. Curr Opin Solid State Mater Sci. 2002;6(3):245-50.
39. Silva NR, Witek L, Coelho PG, Thompson VP, Rekow ED, Smay J. Additive CAD/CAM process for dental prostheses. J Prosthodont. 2011;20(2):93-6.
40. Smay JE, Cesarano Iii J, Lewis JA. Colloidal inks for directed assembly of 3-D periodic structures. Langmuir. 2002;18(14):5429-37.
41. Witek L, Shi Y, Smay J. Controlling calcium and phosphate ion release of 3D printed bioactive ceramic scaffolds: An in vitro study. J Adv Ceram. 2017;6(2):157-64.
42. Zhu C, Smay JE. Thixotropic rheology of concentrated alumina colloidal gels for solid freeform fabrication. J Rheol (Melville, NY, U S). 2011;55(3):655-72.
43. Gupta AR, Walker SB, Lewis JA, editors. Direct-write assembly of 3D periodic ceramic structures2010: American Chemical Society.
44. Haley JL, Alem NM, McEntire BJ, Lewis JA. Force transmission through chest armor during the defeat of .50-caliber rounds. Army Aeromedical Res. Lab.; 1996. Contract No.: Copyright (C) 2019 American Chemical Society (ACS). All Rights Reserved.
45. Lewis JA. Binder removal from ceramics. Annu Rev Mater Sci. 1997;27:147-73.

46. Lewis JA, Bell MA, Busbee TA, Minardi JE, II, inventors; President and Fellows of Harvard College, USA . assignee. Printed three-dimensional (3d) functional part and method of making patent WO2014209994A2. 2014.
47. Ober TJ, Foresti D, Lewis JA. Active mixing of complex fluids at the microscale. Proc Natl Acad Sci U S A. 2015;112(40):12293-8.
48. Rehman Z, Seong K, Lee S, Song MH. Experimental study on the rheological behavior of tetrafluoroethane (R-134a) hydrate slurry. Chemical Engineering Communications. 2018;205(6):822-32.
49. Fair GE, Lange FF. Ceramic Composites with Three-Dimensional Architectures Designed to Produce a Threshold Strength—I. Processing. Journal of the American Ceramic Society. 2005;88(5):1158-64.
50. Hillman C, Suo Z, Lange FF. Cracking of laminates subjected to biaxial tensile stresses. Journal of the American Ceramic Society. 1996;79(8):2127-33.
51. Hbaieb K, McMeeking RM, Lange FF, editors. Modeling crack bifurcation in laminar ceramics. Ceramic Engineering and Science Proceedings; 2008.
52. Pontin MG, Lange FF. Crack bifurcation at the surface of laminar ceramics that exhibit a threshold strength. Journal of the American Ceramic Society. 2005;88(5):1315-7.
53. Wachtman JB, Cannon WB, Matthewson MJ. Mechanical Properties of Ceramics, Second Editon2009. 1-479 p.
54. Ravichandran KS. Elastic Properties of Two-Phase Composites. Journal of the American Ceramic Society. 1994;77(5):1178-84.
55. Ortega JM, Golobic M, Sain JD, Lenhardt JM, Wu AS, Fisher SE, et al. Active Mixing of Disparate Inks for Multimaterial 3D Printing. Advanced Materials Technologies. 2019;4(7).
56. Smay JE, Nadkarni SS, Xu J. Direct writing of dielectric ceramics and base metal electrodes. International Journal of Applied Ceramic Technology. 2007;4(1):47-52.

APPENDICES

Table AI: Measurements of Zirconia Piston-on-3-Ball Samples

Zirconia						
Sample Number	**Thickness (mm)**			**Diameter (mm)**		
1	1.340	1.460	1.380	14.000	14.260	13.980
2	1.380	1.400	1.330	13.920	13.890	13.980
3	1.380	1.400	1.330	13.920	13.890	13.840
4	1.480	1.460	1.460	13.670	13.630	13.640
5	1.380	1.370	1.370	13.660	13.690	13.640
6	1.370	1.380	1.400	13.880	13.790	13.770
7	1.300	1.280	1.340	14.200	14.010	14.190
8	1.340	1.320	1.330	14.010	14.030	13.740
9	1.350	1.330	1.400	13.870	13.810	13.820
10	1.340	1.340	1.300	14.000	14.030	13.940
11	1.410	1.360	1.380	13.900	13.920	13.890
12	1.460	1.360	1.380	13.900	13.920	13.890
13	1.400	1.440	1.390	13.620	13.700	13.650
14	1.360	1.300	1.400	13.840	13.830	13.860
15	1.490	1.480	1.500	13.690	13.740	13.580
16	1.540	1.610	1.550	13.720	13.860	13.650
17	1.590	1.610	1.590	13.990	13.860	13.950
18	1.580	1.550	1.570	13.960	13.890	13.880
19	1.470	1.440	1.510	13.960	13.910	13.840
20	1.560	1.450	1.460	13.910	13.730	13.830

21	1.440	1.440	1.530	13.580	13.650	13.640
22	1.400	1.460	1.450	14.010	14.000	14.020
23	1.520	1.460	1.530	14.160	14.110	14.080
24	1.660	1.690	1.610	13.910	14.030	13.970
25	1.430	1.480	1.420	13.770	13.800	13.730
26	1.490	1.520	1.500	13.730	13.710	13.860
27	1.480	1.490	1.470	13.750	13.770	13.860
28	1.500	1.490	1.490	13.760	13.940	13.720
29	1.510	1.520	1.510	13.660	13.650	13.610
30	1.640	1.640	1.650	14.040	13.920	13.930
31	1.460	1.520	1.460	13.830	13.890	13.880
32	1.450	1.460	1.460	13.600	13.660	13.590
33	1.470	1.490	1.560	13.790	13.760	13.750
34	1.510	1.430	1.440	13.980	13.930	13.930
35	1.510	1.500	1.550	13.670	13.580	13.620
36	1.390	1.390	1.410	13.950	13.990	13.940
37	1.500	1.480	1.490	14.040	13.990	13.860
38	1.460	1.410	1.430	13.740	13.860	13.770
39	1.480	1.480	1.480	13.820	13.750	13.740
40	1.480	1.500	1.560	13.820	13.750	13.740
41	1.420	1.420	1.420	13.670	13.740	13.790

Table AII: Measurements of Alumina Piston-on-3-Ball Samples

Alumina						
Sample Number	**Thickness (mm)**			**Diameter (mm)**		
1	1.340	1.270	1.370	14.770	14.670	14.230
2	1.460	1.470	1.440	13.720	13.740	13.750
3	1.660	1.540	1.540	14.270	13.910	13.810
4	1.460	1.470	1.470	14.360	14.390	14.230

5	1.460	1.470	1.480	13.840	13.820	13.890
6	1.430	1.420	1.430	14.000	14.070	14.120
7	1.430	1.370	1.430	14.090	14.090	14.130
8	1.440	1.440	1.430	14.040	14.000	14.020
9	1.530	1.520	1.530	13.850	13.930	13.950
10	1.410	1.390	1.400	13.780	13.850	13.720
11	1.490	1.410	1.470	14.820	14.290	14.380
12	1.400	1.370	1.380	14.170	14.180	14.110
13	1.470	1.530	1.480	14.170	14.180	14.150
14	1.340	1.360	1.390	13.850	13.760	13.860
15	1.540	1.510	1.560	13.840	14.000	13.930
16	1.360	1.430	1.400	14.020	14.100	14.060
17	1.430	1.390	1.420	13.890	13.970	13.920
18	1.360	1.340	1.360	14.840	14.610	14.610
19	1.400	1.400	1.400	13.790	13.690	13.690
20	1.290	1.370	1.390	14.010	13.900	13.900
21	1.320	1.370	1.370	13.930	13.840	13.810
22	1.320	1.370	1.430	13.740	13.780	13.780
23	1.350	1.370	1.350	13.880	13.820	13.870
24	1.370	1.380	1.390	13.810	13.830	13.810
25	1.390	1.360	1.350	13.710	13.630	13.620
26	1.280	1.310	1.300	13.810	13.710	13.710
27	1.310	1.320	1.290	13.790	13.870	13.840
28	1.260	1.290	1.280	13.760	13.860	13.790
29	1.240	1.260	1.220	13.860	13.970	13.940
30	1.270	1.270	1.300	14.020	14.000	13.920

Table AIII: Measurements of ASZ Piston-on-3-Ball Samples

ASZ						
Sample Number	Thickness			Diameter		
1	1.340	1.380	1.33	13.75	13.780	13.750
2	1.480	1.380	1.38	13.55	13.580	13.470
3	1.380	1.400	1.4	13.51	13.450	13.480
4	1.380	1.380	1.36	13.68	13.680	13.620
5	1.400	1.400	1.38	13.72	13.680	13.710
6	1.420	1.430	1.44	13.54	13.440	13.450
7	1.530	1.350	1.38	13.73	13.760	13.790
8	1.440	1.440	1.4	13.58	13.580	13.500
9	1.350	1.390	1.37	13.63	13.700	13.640
10	1.360	1.340	1.37	13.81	13.770	13.740
11	1.410	1.400	1.43	13.48	13.490	13.420
12	1.390	1.380	1.38	13.57	13.520	13.550
13	1.400	1.370	1.38	13.79	13.720	13.730
14	1.380	1.440	1.42	13.51	13.590	13.510
15	1.340	1.360	1.35	13.92	13.950	13.910
16	1.420	1.430	1.4	13.65	13.590	13.570
17	1.420	1.420	1.41	13.58	13.650	13.490
18	1.390	1.390	1.38	13.76	13.800	13.890
19	1.420	1.440	1.44	13.5	13.450	13.500
20	1.420	1.460	1.46	14.63	14.720	14.520
21	1.490	1.350	1.45	14.68	14.590	14.520
22	1.420	1.390	1.47	14.57	14.590	14.520
23	1.540	1.400	1.38	14.85	14.820	14.720
24	1.420	1.390	1.39	14.11	14.080	14.050
25	1.460	1.490	1.4	14.59	14.310	14.510
26	1.520	1.450	1.49	14.29	14.080	14.070
27	1.430	1.370	1.48	14.17	14.360	14.570

28	1.450	1.520	1.49	14.26	14.440	14.490
29	1.480	1.450	1.47	14.45	14.430	14.230
30	1.510	1.500	1.400	14.400	14.390	14.450
31	1.460	1.470	1.470	14.240	14.270	14.190
32	1.450	1.510	1.380	14.730	15.100	14.720
33	1.440	1.480	1.530	14.280	14.020	14.090
34	1.460	1.400	1.470	14.160	14.040	14.220
35	1.520	1.410	1.430	14.110	14.110	14.180
36	1.480	1.460	1.440	14.170	14.140	14.210

Table AIV: Measurements of CS Piston-on-3-Ball Samples

CS						
Sample Number	**Thickness**			**Diameter**		
1	1.369	1.397	1.370	14.425	14.561	14.502
2	1.291	1.305	1.347	14.576	14.437	14.532
3	1.324	1.337	1.359	14.604	14.719	14.704
4	1.382	1.396	1.396	14.293	14.498	14.323
5	1.576	1.240	1.304	14.913	14.942	15.000
6	1.375	1.381	1.395	14.320	14.432	14.341
7	1.155	1.232	1.194	14.765	14.897	14.837
8	1.374	1.378	1.401	14.244	14.209	14.301
9	1.385	1.428	1.342	14.669	14.693	14.650
10	1.449	1.405	1.431	14.464	14.460	14.490
11	1.367	1.343	1.389	14.790	14.700	14.760
12	1.289	1.330	1.300	13.977	13.943	13.950
13	1.329	1.407	1.388	14.477	14.654	14.402
14	1.281	1.350	1.303	15.062	14.851	14.790
15	1.388	1.379	1.365	14.297	14.451	14.409
16	1.497	1.491	1.518	13.973	13.870	14.135

17	1.357	1.350	1.423	14.641	14.466	14.433
18	1.455	1.362	1.324	14.922	14.968	14.915
19	1.403	1.402	1.394	14.270	14.465	14.464
20	1.330	1.228	1.256	14.784	14.876	15.042
21	1.427	1.371	1.380	14.210	14.134	14.239
22	1.448	1.380	1.394	14.092	13.996	14.019
23	1.345	1.357	1.371	14.355	14.455	14.432
24	1.414	1.370	1.389	14.585	14.578	14.755
25	1.417	1.364	1.327	14.822	14.531	14.655
26	1.434	1.461	1.415	14.685	14.671	14.557
27	1.377	1.383	1.403	13.928	14.164	13.996
28	1.355	1.363	1.419	14.351	14.511	14.294
29	1.379	1.360	1.361	14.662	14.521	14.431
30	1.497	1.504	1.491	13.948	13.824	14.060
31	1.360	1.438	1.335	14.460	14.646	14.461
32	1.370	1.381	1.380	14.667	14.551	14.716
33	1.349	1.351	1.298	14.775	14.844	14.780
34	1.459	1.474	1.471	14.048	13.877	13.931

VITA

Morgan Cornish

Candidate for the Degree of Master of Science

EDUCATION

Master of Science (May 2020) in Materials Science in Engineering, Oklahoma State University, Tulsa, OK. Thesis title: “Threshold strength ceramic dental crowns by direct ink writing.”

Bachelor of Science (May 2018) in Ceramic Engineering, Missouri University of Science and Technology, Rolla, MO.

ACADEMIC EMPLOYMENT

Graduate Research Assistant, Department of Materials Science and Engineering, Oklahoma State University, Aug 2018 –May 2019. Research activities included general lab upkeep, facility and equipment care, design and manufacturing of equipment, and thesis research.

Graduate Teaching Assistant, Department of Mechanical and Aerospace Engineering, Oklahoma State University, Aug 2019 –May 2020. Teaching activities included teaching labs, grading, and tutoring.

ACADEMIC AWARDS

Doyle & Becky Young Endowed Graduate Fellowship, College of Engineering, Architecture & Technology, Oklahoma State University. Aug 2019.

PROFESSIONAL MEMBERSHIP

HRC Graduate Student Organization –Vice President
Materials Research Society
Keramos
Materials Advantage